

# CIRCUMSTELLAR DISK CANDIDATES IDENTIFIED FROM ULTRAVIOLET EXCESSES IN THE ORION NEBULA CLUSTER FLANKING FIELDS

L. M. REBULL,<sup>1,2</sup> L. A. HILLENBRAND,<sup>3</sup> S. E. STROM,<sup>4</sup> D. K. DUNCAN,<sup>1</sup> BRIAN M. PATTEN,<sup>2,5</sup> C. M. PAVLOVSKY,<sup>2,6</sup>  
 R. MAKIDON,<sup>6</sup> AND MARK T. ADAMS<sup>7</sup>

Received 1999 October 15; accepted 2000 March 2

## ABSTRACT

We present an optical study of four  $45' \times 45'$  fields centered  $\sim 0.5^\circ$  east, west, north, and south of the Orion Nebula Cluster center. We have measured  $V$  and  $I_C$  photometry for  $\sim 5000$  stars, and  $U$  photometry for  $\sim 1600$  of these. We have obtained spectral classifications for  $\sim 300$  of the stars with  $UVI_C$  photometry plus an additional  $\sim 200$  stars located outside the area of our photometric survey. Dereddened photometry allows us to investigate the evidence for circumstellar accretion disks from excess emission at ultraviolet wavelengths, as well as the mass and age distributions of our sample. We find  $\sim 230$  active accretion disk candidates and estimate the accretion disk fraction at  $\gtrsim 40\%$ . We use the magnitude of the ultraviolet excess to infer disk accretion rates. The mass accretion rate ( $\dot{M}$ ) decreases slowly with age over the limited age range spanned by our data, 1–3 Myr, and increases slowly with mass over the limited mass range  $0.2\text{--}1.2 M_\odot$ . Although complicated selection effects are likely to affect the overall trends with mass and age, we are sensitive to, but do not see, high  $\dot{M}$ -values associated with the older ages and lower masses in our sample. The mean value of  $\dot{M}$  is  $\sim 10^{-8} M_\odot \text{ yr}^{-1}$ , with a range of more than 1 order of magnitude at all ages and masses. We find an age and age spread for our sample of  $10^{6.0 \pm 0.4} \text{ yr}$  with no variation within or between our fields. Meaningful constraint of the mass distribution is precluded because of the completeness limits of our survey.

*Key words:* stars: pre-main-sequence

## 1. INTRODUCTION

Most, if not all, stars are suspected of having circumstellar accretion disks at birth. Interaction between the accretion disk and star, particularly as the star evolves and the disk dissipates, is still not well understood, and it bears specifically on issues of planet formation (see, e.g., Hollenbach et al. 2000) and angular momentum evolution (e.g., Stassun et al. 1999; Herbst et al. 2000; Rebull 2000).

Investigators have used a variety of methods for identifying circumstellar accretion disks and measuring mass accretion rates (Calvet et al. 2000), including infrared-excess, optical spectroscopic emission-line, and ultraviolet-excess techniques. The efficacy of these different methods is dictated by the contrast between any excess emission and the photospheric emission, which in turn depends on the stellar mass and radius, the disk mass and mass accretion rate, and the orientation of the star-disk system with respect to the observer.

Infrared excess originates from dust heated both by reprocessed starlight and by viscous dissipation of accretion

energy within the disk. *JHK*L photometry is commonly used to infer the presence of disks. IR-excess techniques are most effective for higher mass stars, where the contrast between disk and star is high, and least effective for lower mass stars, where the contrast between a cold disk and cool photosphere is low. This method also suffers from inclination effects and from the effects of inner disk holes thought to be formed by the stellar magnetosphere.

Spectroscopic emission lines are produced in the outflows and inflows thought to be associated with the accretion process (see, e.g., Calvet et al. 2000; Najita et al. 2000).  $H\alpha$  surveys using, e.g., objective-prism, slit, or fiber spectroscopy have long been used to identify young stars. In the context of the current paradigm,  $H\alpha$  luminosity is directly related to disk mass accretion rate (e.g., Najita et al. 2000). At constant stellar age, a given mass accretion rate produces a higher  $H\alpha$  equivalent width among late-type, low-mass stars compared with early-type, high-mass counterparts. The use of  $H\alpha$  as a diagnostic is compromised in regions where strong background nebular emission can complicate determination of the  $H\alpha$  equivalent width, as in the Orion Nebula region.

Ultraviolet/optical excess originates from energy released in accretion hot spots as inflowing material is channeled by the stellar magnetic field onto the star at high latitudes and/or in the boundary layer between the disk and the star. UV excesses historically have been used to identify young stars (Haro & Herbig 1955; Walker 1956) and study accretion disks (e.g., Bertout et al. 1988; Basri & Bertout 1989; Hartigan et al. 1991), but because of the relative faintness of late-type stellar photospheres in  $U$  coupled with the increased significance of reddening corrections, this disk detection method is less commonly used than the others. At constant age and fixed mass accretion rate, the contrast between the excess and the photosphere in the UV is highest for late spectral type, low-mass stars and lowest for high-

<sup>1</sup> Department of Astronomy and Astrophysics, University of Chicago, 5640 South Ellis Avenue, Chicago, IL 60637; rebull@oddjob.uchicago.edu.

<sup>2</sup> Visiting Astronomer, Kitt Peak National Observatory, National Optical Astronomy Observatories, operated by the Association of Universities for Research in Astronomy, Inc., under cooperative agreement with the National Science Foundation.

<sup>3</sup> Department of Astronomy, California Institute of Technology, Pasadena, CA 91125.

<sup>4</sup> National Optical Astronomy Observatories, 950 North Cherry Avenue, Tucson, AZ 85726.

<sup>5</sup> Harvard-Smithsonian Center for Astrophysics, 60 Garden St., Cambridge, MA 02138.

<sup>6</sup> Space Telescope Science Institute, 3700 San Martin Drive, Baltimore, MD 21218.

<sup>7</sup> McDonald Observatory, University of Texas, P.O. Box 1337, Fort Davis, TX 79734-1337.

TABLE 1  
OBSERVATIONS I: STARS IN THE ORION LOCUS

Star	Field	R.A. <sup>a</sup>	Decl. <sup>a</sup>	$I_C$	$\sigma_I$	$(V - I_C)$	$\sigma_{(V-I)}$	$(U - V)$	$\sigma_{(U-V)}$	Type	$A_I$	$A_V$
1.....	1	5 31 24.6	-5 26 42.0	14.15	0.03	2.44	0.04	2.75	0.05	...	...	...
2.....	1	5 31 25.8	-5 05 15.6	14.28	0.06	2.11	0.07	2.94	0.07	...	...	...
3.....	1	5 31 26.3	-5 36 37.3	12.57	0.01	2.67	0.02	2.54	0.02	M4:	-0.31	-0.50
4.....	1	5 31 27.1	-5 10 29.0	12.50	0.03	1.18	0.03	1.89	0.04	...	...	...
5.....	1	5 31 30.4	-5 37 58.7	17.32	0.03	3.44	0.06	...	...	...	...	...

NOTES.—Photometry and spectral types (when available) for stars in the Orion locus. Table 1 is presented in its entirety in the electronic edition of the *Astronomical Journal*. A portion is shown here for guidance regarding its form and content.

<sup>a</sup> J2000.0 coordinates, good to at least  $\sim 2''$ . Units of right ascension are hours, minutes, and seconds, and units of declination are degrees, arcminutes, and arcseconds.

TABLE 2  
OBSERVATIONS II: APPARENT FIELD STARS WITH SPECTRA

Star	Field	R.A. <sup>a</sup>	Decl. <sup>a</sup>	$I_C$	$\sigma_I$	$(V - I_C)$	$\sigma_{(V-I)}$	$(U - V)$	$\sigma_{(U-V)}$	Type	$A_I$	$A_V$
1.....	1	5 31 29.7	-5 31 28.6	12.73	0.01	1.07	0.02	1.18	0.02	G2:	0.55	0.90
2.....	1	5 31 29.7	-5 08 52.6	17.43	0.04	1.60	0.05	...	...	K0:	1.16	1.88
3.....	1	5 31 43.9	-5 24 21.0	12.31	0.01	0.87	0.01	1.24	0.01	G0	0.26	0.43
4.....	1	5 31 57.4	-5 37 07.4	13.26	0.02	1.30	0.03	1.60	0.04	K2:	0.59	0.95
5.....	1	5 31 58.4	-5 35 11.7	15.47	0.03	1.95	0.04	2.76	0.09	G2	1.96	3.18

NOTES.—Photometry and spectral types (when available) for stars in the Orion locus. Table 2 is presented in its entirety in the electronic edition of the *Astronomical Journal*. A portion is shown here for guidance regarding its form and content.

<sup>a</sup> J2000 coordinates, good to at least  $\sim 2''$ . Units of right ascension are hours, minutes, and seconds, and units of declination are degrees, arcminutes, and arcseconds.

mass, early-type stars. Recently, Gullbring et al. (1998) and Hartmann et al. (1998) have exploited this advantage and used  $U$ -band excesses to estimate mass accretion rates,  $\dot{M}$ , for low-mass stars in the Taurus-Auriga and Chameleon star-forming regions.

In this paper, we continue the type of analysis introduced by Gullbring et al. (1998) and Hartmann et al. (1998), using UV excesses to identify active accretion disk candidates in the outer regions of the Orion Nebula Cluster. We estimate from a simple model that UV photometry is sensitive to mass accretion rates  $\gtrsim 10^{-9} M_\odot \text{ yr}^{-1}$  for stars of 1 Myr and  $0.1 M_\odot$ , and  $\gtrsim 10^{-7.5} M_\odot \text{ yr}^{-1}$  for stars of 1 Myr and  $1 M_\odot$ .

We present a new optical photometric and spectroscopic database for young stars located in four  $45' \times 45'$  fields centered  $\sim 0.5^\circ$  east, west, north, and south of the Orion Nebula Cluster center, which we refer to as the Orion Nebula Cluster flanking fields. After describing the observations and data reduction (§ 2) and the basic observational results (§ 3), we discuss dereddening of the photometry (§ 4). Following that, we review the star-forming history of our regions (§ 5). We then discuss in some detail our selection of accretion disk candidates (§ 6), including the distribution of observed UV excesses and any possible systematics due to chromospheric activity, reddening, or intrinsic color uncertainties. We arrive at mass accretion rates (§ 7), which we correlate with stellar mass and age, and then the disk fraction (§ 7.5). Finally, we summarize our major conclusions (§ 8).

These new data contribute statistics for problems such as whether or not the characteristics of disks are the same around stars of different masses and, as the disks dissipate and angular momentum is transferred, how  $\dot{M}$  decreases with age. A forthcoming paper (Rebull 2000) will specifically address the relationship between disks and angular momentum for stars in the current sample.

## 2. OBSERVATIONS AND DATA REDUCTION

As part of a larger study of angular momentum evolution in young, low-mass stars, we have surveyed four fields in the outer Orion Nebula Cluster (ONC), surrounding but not including the Trapezium region. Each of the fields is  $45'$  square; see Figure 1. Time series photometry has been obtained for these four fields using the McDonald Observatory 0.76 m telescope. Light curves will be discussed in subsequent papers starting with Rebull (2000). In 2.75 of the fields, we obtained well-calibrated  $VI_C$  photometry for a total of  $\sim 5000$  stars, and  $U$  photometry for  $\sim 1600$  of these. Across all four fields we obtained spectroscopy at classification resolution for a total of  $\sim 500$  targets (410 of which are classifiable),  $\sim 300$  of which are found in the 2.75 fields with  $(U)VI_C$  photometry.

Observations are presented in Tables 1, 2, and 3. Coordinates presented here are good to at least  $\sim 2''$  and are based on the *Hubble Space Telescope* Guide Star Catalog (Lasker

TABLE 3  
OBSERVATIONS III: STARS WITH SPECTROSCOPY ONLY

Star	Field	R.A. <sup>a</sup>	Decl. <sup>a</sup>	Type
1.....	1	5 31 32.5	-5 17 50.12	K2:
2.....	1	5 31 34.2	-5 01 01.92	K1
3.....	1	5 31 40.5	-5 19 23.84	K0:
4.....	1	5 32 11.3	-5 37 44.12	M0
5.....	1	5 32 51.8	-5 35 25.39	M5:

NOTES.—Photometry and spectral types (when available) for stars in the Orion locus. Table 2 is presented in its entirety in the electronic edition of the *Astronomical Journal*. A portion is shown here for guidance regarding its form and content. Units of right ascension are hours, minutes, and seconds, and units of declination are degrees, arcminutes, and arcseconds.

<sup>a</sup> J2000.0 coordinates, good to at least  $\sim 2''$ .

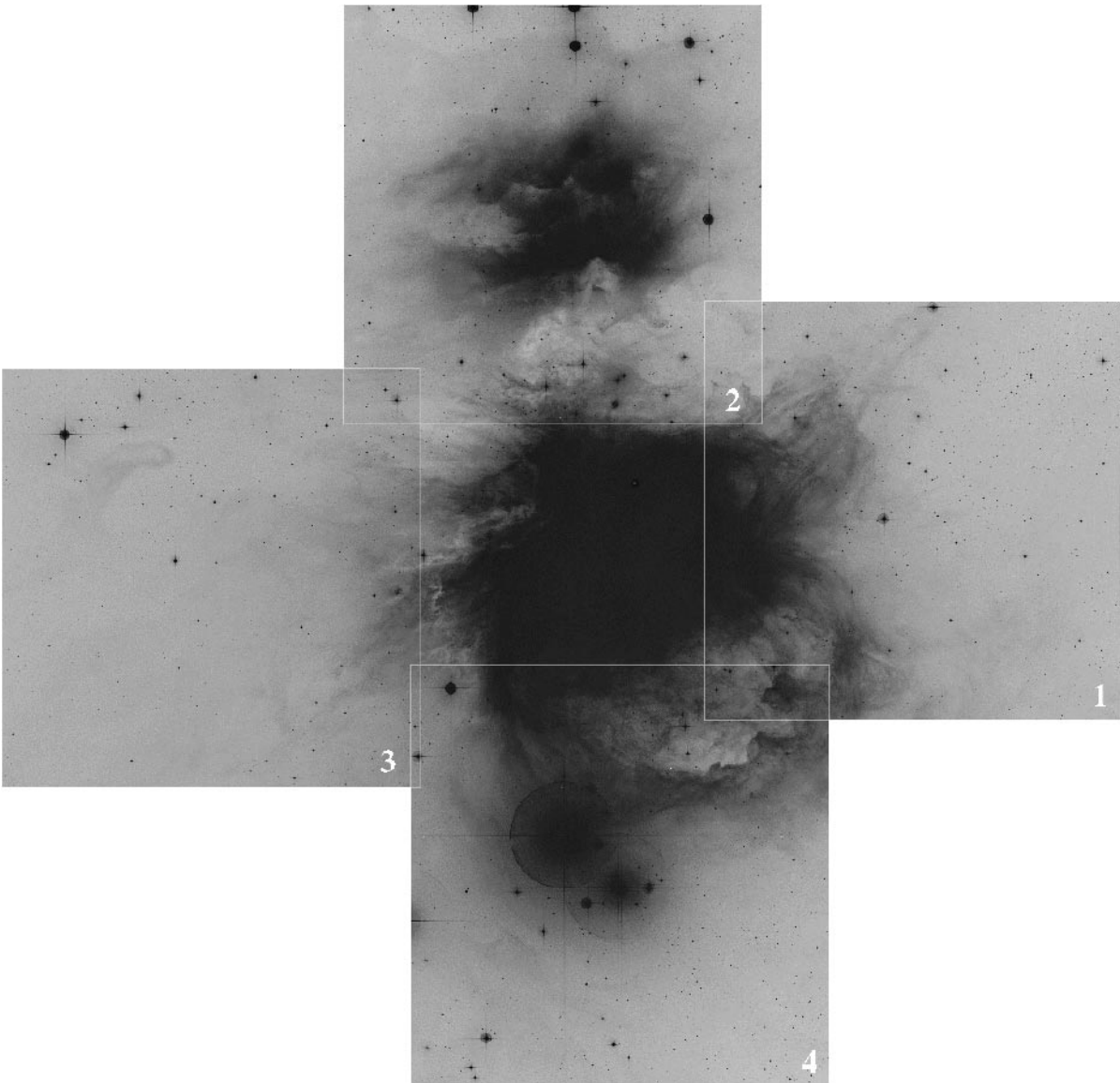


FIG. 1.—Digitized Sky Survey images (from STScI) illustrating the relative placement of the Orion Nebula Cluster flanking fields, numbered 1–4. Note that the Trapezium region is not included in our survey area. Time series photometry for stars in each of these 45' fields will be presented in Rebull (2000). Optical photometry and spectroscopy are discussed in this paper.

et al. 1988). Photometric and spectroscopic accuracy is discussed below. We summarize the distribution of photometric and spectroscopic data by wavelength and by field in Tables 4 and 5.

2.1. *UVI<sub>C</sub> Photometry*

We obtained *U*, *V*, and Cousins *I* (*I<sub>C</sub>*) photometry in 1998 January with the KPNO 0.9 m telescope. Our images

are 23' on a side at a plate scale of 0".68 pixel<sup>−1</sup>. As a result of weather and instrumental complications, field 3 was not observed at all, nor was the northwestern quadrant of field 4. In the remaining 2.75 fields, we obtained images in all three colors. In *U*, three frames were taken to allow for cosmic-ray rejection, each 20 minutes long. In *V*, two frames were taken, 30 s and 600 s; in *I<sub>C</sub>*, 15 s and 300 s exposures were taken. On most nights we also imaged stan-

TABLE 4  
STAR COUNT SUMMARY: ALL STARS

Field	<i>UVI<sub>C</sub></i> Photometry	<i>VI<sub>C</sub></i> Photometry	Total Photometry	Spectral Types	Uncertain Spectra <sup>a</sup>	Total Spectra	<i>UVI<sub>C</sub></i> and Spectral Types	<i>VI<sub>C</sub></i> and Good Spectra
1 .....	671	1210	1881	98	19	117	64	23
2 .....	544	1258	1802	116	10	126	77	38
3 .....	...	...	...	109	14	123	...	...
4 .....	349	760	1109	117	9	126	42	24
Total .....	1564	3228	4792	440	52	492	183	85

<sup>a</sup> Reported here for completeness and included in Tables 1–3 above, but not used in analysis discussed in paper.

TABLE 5  
STAR COUNT SUMMARY: ORION LOCUS

Field	$UVI_C$ Photometry	$VI_C$ Photometry	Total Photometry	$UVI_C$ and Spectral Types	$VI_C$ and Spectral Types
1 .....	180	207	387	54	21
2 .....	335	377	712	73	35
3 .....	...	...	...	...	...
4 .....	211	310	521	39	22
Total .....	726	894	1620	166	78

standard fields from Landolt (1992). We were unable to obtain any standards on the night we observed field 4, so we used standards from the previous night; examination of the resulting photometry suggests that atmospheric conditions did not change substantially between nights.

Standard IRAF procedures were used for bias subtraction and flat-fielding. IRAF aperture photometry from the DAOPHOT package was used for photometry extraction. Although a few of the stars have close apparent companions, the stellar density is generally low enough to make aperture photometry acceptable. The IRAF routine MKAPFILE was used to determine and apply aperture corrections based on ensemble averages of stars in each separate frame.

Photometric errors are a combination of photon noise, CCD noise sources, centering errors, aperture corrections, errors in the extinction corrections, and errors in the color corrections. Formal net error on all but photon and CCD noise were determined to be  $\pm 0.01$  mag. Measurements were retained if the net error ( $\pm 0.01$  added in quadrature to the error from photon and CCD noise) in color was  $\leq 0.1$  mag. Given this restriction, over all fields,  $\sim 5000$  stars have reported  $V$  and  $I_C$  magnitudes, and  $\sim 1600$  of those have reported  $U$  magnitudes. The limiting magnitudes of the population of stars with good measurements at all three of  $UVI_C$  are  $U \sim 20$ ,  $V \sim 17.5$ , and  $I_C \sim 16.5$ . For the fainter population with good  $V$  and  $I_C$  magnitudes but for which  $U$  is below our detection threshold, the limiting magnitudes are  $V \sim 20$  and  $I_C \sim 18$ .

## 2.2. Spectroscopy

Low-resolution classification spectra were obtained using the WIYN<sup>8</sup> 3.5 m telescope and the Hydra fiber-optic echelle through the NOAO WIYN queue program in fall 1997. Stars were selected for spectroscopic observation not from the photometric database just described, but on the basis of whether or not they showed photometric variability in the time series observations described in Rebull (2000). The spectroscopic sample is thus biased toward variable stars but also includes some nonvariables ( $\sim 15\%$ ) in order to use as many of the Hydra fibers as possible. Of the stars selected as variable, the distribution of standard deviations of the light curves is strongly peaked with a long tail; the mode is  $\sigma \sim 0.02$ , with a tail up to  $\sim 0.5$ . Of the stars selected as nonvariable “filler,” the mode is  $\sigma \sim 0.01$ , with a tail to only  $\sim 0.1$ .

Two fiber configurations were taken per field, with three 10 minute exposures for the brighter stars and three half-

hour exposures for the fainter stars. The standard IRAF Hydra software pipeline DOHYDRA was used to process these data. Signal-to-noise ratios of the reduced spectra vary as a result of fiber placement and transmission but are typically  $\sim 40$ , and about 7% of them are  $\geq 70$ . We obtained about 500 total spectra (over all four fields) at a resolution of  $5 \text{ \AA}$ , yielding usable data over the range  $5000\text{--}9300 \text{ \AA}$ .

## 3. BASIC OBSERVATIONAL RESULTS

Figure 2 shows the  $(I_C, V - I_C)$  color-magnitude diagram (CMD) for all  $\sim 5000$  stars with  $V$  and  $I_C$  measurements. These data have not been corrected for reddening, although a vector indicating the direction and slope of typical reddening (as derived in § 4) is shown for reference. The zero-age main sequence (ZAMS) includes measurements from Bessell (1991), Leggett (1992), and Leggett, Allard, & Hauschildt (1998). We transformed the limiting magnitudes of  $U = 20$  and  $V = 20$  into the  $(I_C, V - I_C)$ -plane; however, because these transformations are based on ZAMS colors, stars fainter than this can be detected in our sample if they have photometric excesses at the shorter wavelengths due to accretion.

A gap between the pre-main-sequence (PMS) Orion member stars and the field stars can be seen clearly. We use a line with slope 2.13 and intercept 10.3 to divide the  $(I_C, V - I_C)$  CMD into possible Orion members (located above

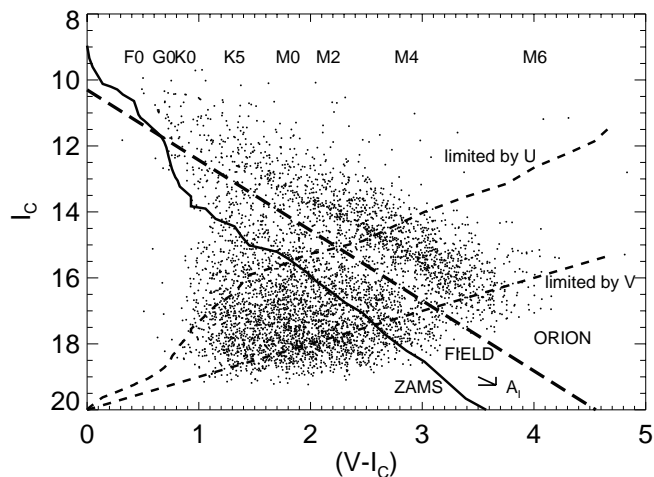


FIG. 2.—Observed color-magnitude diagram for all of the photometry, over the three fields (1, 2, 4) for which photometry was obtained. The gap between the PMS stars in Orion and the field stars can be seen clearly; lines indicating our adopted cutoff (long-dashed line) and the ZAMS (solid line) are indicated. The reddening vector for  $A_I = 0.25$  ( $A_V = 0.41$ ) is included in the lower right corner. Short-dashed lines are the completeness limits in  $U$  and  $V$ , calculated using our measured sensitivity combined with main-sequence colors.

<sup>8</sup> The WIYN Observatory is a joint facility of the University of Wisconsin–Madison, Indiana University, Yale University, and the National Optical Astronomy Observatories.

this line) and probable field stars (located below the line). Note that this line closely parallels the reddening vector. Membership studies toward Orion (Parenago 1954; Jones & Walker 1988; van Altena et al. 1988; McNamara et al. 1989; Tian et al. 1996) generally have focused on the inner Trapezium region, with little proper-motion information available for stars in the larger region studied here and essentially none for stars fainter than  $V \sim 13$ . Thus, we have used the line drawn through the gap in Figure 2 as a provisional indication of membership and dropped all stars below it from the following analysis. By so doing, we may exclude some older Orion member stars (if such a population exists) and possibly include some field stars (especially background giants). This cut reduces the total number of stars such that  $\sim 1500$  stars with  $V-I_C$  photometry remain,  $\sim 700$  of which have  $U$  measurements. This subsample hereafter will be referred to as the “Orion locus.”

Figure 3 presents the observed color-color diagram for those stars with  $UVI_C$  photometry found in the Orion locus of Figure 2. There are a few stars located below the ZAMS relation that can be dereddened to intersect the ZAMS. Our focus for the majority of this paper, however, is the many more stars located high enough in this diagram that they cannot be dereddened to intersect the ZAMS; these are the UV-excess stars.

A subsample of the stars in Figures 2 and 3 have optical spectroscopy, which we combine with the photometry in § 4 to derive individual extinction values, as well as the modal or most likely reddening. We classified our spectra using the Allen & Strom (1995) classification standards, which are specifically for this spectral region and instrumental setup, supplemented with the Kirkpatrick et al. (1991) late, M standards. Each spectrum was classified by two different authors, for a total of four passes through the data. We took into account the fact that optical spectra of young PMS stars show signs of lower surface gravity than the main-sequence classification standards, especially for spectral types M4 and later. We note, however, that the colors of these late-type stars appear closer to dwarfs than to giants (Walter et al. 1994) despite the intermediate gravity spectra.

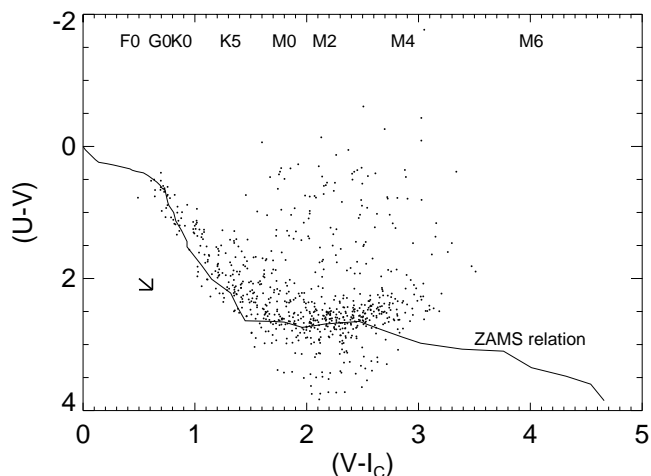


FIG. 3.—Observed color-color diagram for stars in the Orion locus as defined in Fig. 2. Lines indicating the color-color relation found on the ZAMS and the reddening vector for  $A_V = 0.25$  ( $A_U = 0.41$ ) are indicated. There are a significant number of stars with large  $U-V$  excesses whose positions cannot be explained by reddening; note the star with  $U-V \sim -2$ .

We estimate classification accuracy to two subclasses for the earliest types (A, F, and G), to one subclass for the K stars, and to less than a subclass for the M stars. In addition to the gravity issue, spectral classification is complicated by veiling and by interstellar reddening, as well as by the accuracy of nebular subtraction achieved with fiber spectrographs. Errors from nebular subtraction and veiling are difficult to quantify but are likely to have a systematic effect in the same direction of making the classifications earlier than they should be, although with a magnitude of less than a subclass unless veiling is extreme.

Figure 4 shows a histogram of the derived spectral types. Of the 410 stars with classifiable spectra, five are A stars, 17 F stars, 17 G stars, 141 (34%) K stars, and 230 (56%) M stars. About 50 more stars with uncertain types are not plotted here but are reported in Table 1. Note that the spectral classifications cover all four fields of Figure 1, whereas the photometry covers only 2.75 fields; about 300 of the spectroscopic targets fall in the regions where we have photometry (see Tables 4 and 5).

How representative is the spectroscopic data set of all stars in the Orion locus? We can quantify the degree to which the spectroscopic sample represents the photometric sample of candidate Orion members in two ways. First, we compare the location of stars from each sample in the color-magnitude diagram; second, we compare their spatial distributions.

Figure 5 highlights the stars with spectroscopy in the CMD. The relative density of squares and dots in this figure suggests that the photometric and spectroscopic populations *within the Orion locus* cover the same regions of the CMD. Of the  $\sim 5000$  stars in this diagram, 244 have spectral classifications, with 210 being in the Orion locus. The subset of stars with  $U$  magnitudes includes 166 with spectral classifications, 142 of which fall within the Orion locus. Strong bias of the squares in this figure towards the Orion locus suggests that our selection of candidates for spectroscopy based on photometric variability has preferentially selected young candidate members of Orion, as one might naively expect.

Figure 6 presents the fraction of stars in the Orion locus with spectroscopy, as a function of position and color. The spectroscopic sample is unambiguously constant with

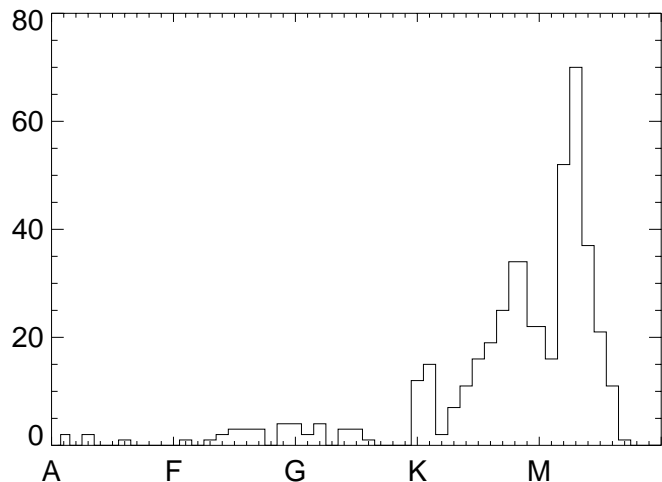


FIG. 4.—Histogram of all 410 classifiable stars over all four fields; 141 (34%) are K stars, and 230 (56%) are M stars.

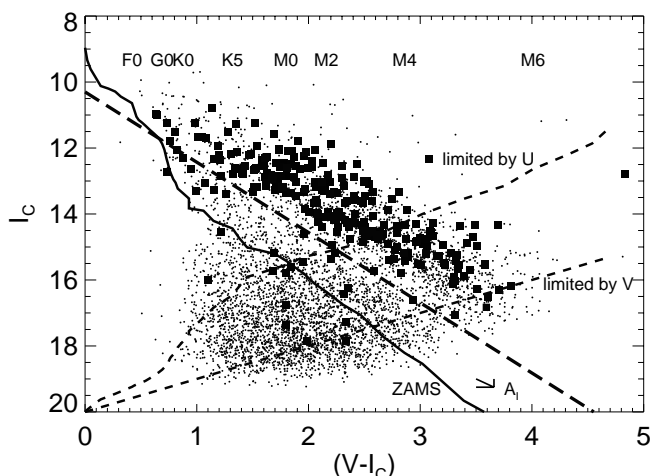


FIG. 5.—Observed CMD for all photometry. Notation is as in Fig. 2 except that squares indicate the stars for which classification spectra exist. The relative density of squares and dots in this figure suggests that the photometric and spectroscopic populations cover the same regions of the CMD within the Orion locus. The spectroscopic sample is composed largely of candidate Orion members.

radial distance from  $\theta$  Ori. The photometric survey starts to become incomplete at  $V-I_C \sim 3$ , but blueward of that, the distribution across all bins but one is flat within the error bars. There is an apparent overdensity of stars with spectra near  $V-I_C \sim 1.6 \pm 0.5$ , amounting to a factor of 2, but the error bars overlap with those in adjacent bins. With this possible exception the spectroscopic sample seems drawn in a representative fashion from stars in the Orion locus. This is not a critical point, however, given that one of our primary goals is to derive mass accretion rates as a function of mass and age, not to derive the mass and age distributions.

#### 4. REDDENING CORRECTIONS

The first step in our analysis is to derive the extinction (measured here as  $A_I$ ) toward each star in our sample. This can be done on an individual basis for those stars with both photometry and spectroscopy. We compare observed stellar

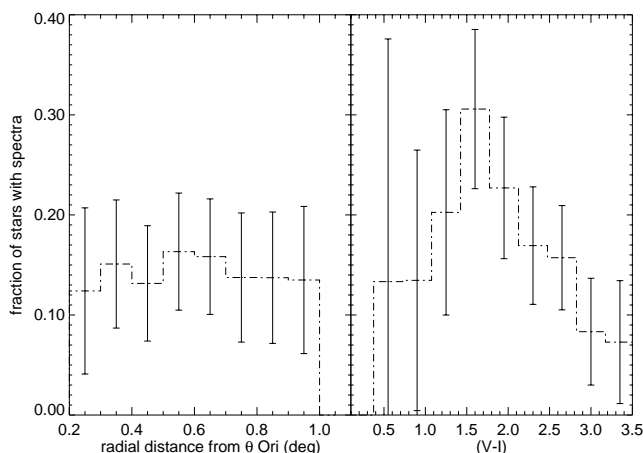


FIG. 6.—Fraction of stars with spectral types as a function of radial distance from  $\theta$  Ori (center of Trapezium) and  $V-I_C$ . Only stars from the Orion locus are included. Error bars are calculated from Poisson statistics. The fraction of stars with spectral types is unambiguously constant with radial distance from  $\theta$  Ori; the fraction is essentially constant with  $V-I_C$ .

colors with those expected based on spectral classification to obtain estimates of color excesses. The wavelength that is thought to minimize the contribution from non-photospheric sources is  $\sim 8000 \text{ \AA}$ , and thus young optically visible PMS stars are usually best dereddened using spectral types and the color index  $R-I_C$ . However, in the specific case of Orion, there is very strong nebular contamination in  $R$  due to  $H\alpha$  emission, so we must use the  $V-I_C$  index instead. Dereddening relationships used were  $A_I = 1.61E(V-I_C)$  and  $E(U-V) = 1.45E(V-I_C)$  (Fitzpatrick 1999; E. Fitzpatrick 1999, private communication).

We show in Figure 7a the extinction distribution derived for the spectroscopic sample. The shape of this histogram does not change significantly between the three fields studied (they are combined here to improve the statistics), nor does inclusion of the few stars not in the Orion locus have any effect. Note that there are some unphysical (i.e., negative) values of  $A_I$ . Most of these negative values of  $A_I$  are found for stars of the latest types; all but two of the  $\sim 30$  late-M stars ( $> M4$ ) result in negative  $A_I$ -values. These young late-M stars are apparently bluer than expected; we will discuss the possible reasons for this below (§ 6.4), but note here that this blueness problem for late spectral types is not unique to this study.

In deriving a most probable value for the reddening, we mitigate problems with uncertain spectral types for G stars and earlier and with apparent blueness of late-M stars, by considering a sample of Orion locus stars in the range K0–K7. Figure 7b presents the histogram of extinction values for stars in this range, which is sharply peaked. The peak has changed by  $\lesssim 0.1$  mag from the full sample to the restricted K0–K7 sample (Figs. 7a and 7b). We take the most likely extinction value (mode of this histogram) to be  $A_I = 0.25$ .<sup>9</sup> The corresponding most likely reddening values are  $E(V-I) = 0.12$  and  $E(U-V) = 0.17$ .

<sup>9</sup> We note that our typical reddening value,  $A_I = 0.25$  or  $A_V = 0.41$ , is much less than that found in Trapezium,  $A_V = 1.5$  (Hillenbrand 1997). This is likely to reflect the fact that our stars are more than  $\sim 3$  pc in projection from the narrow ridge of molecular material associated with Trapezium.

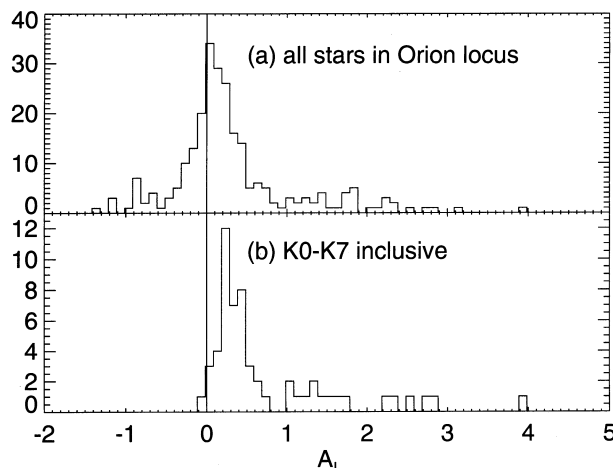


FIG. 7.—Histogram of derived  $A_I$ -values: (a) all 244 stars in the Orion locus with spectral classifications and  $VI_C$  photometry; (b) just 57 stars between K0 and K7, inclusive. From this figure, we infer that the most likely reddening value is  $A_I = 0.25$  ( $A_V = 0.41$ ) with a  $\pm 1 \sigma$  width of 0.1 mag.

Now, since we have shown that the spectroscopic sample is representative of the photometric sample within the Orion locus, the strongly peaked  $A_I$  distribution allows us to increase dramatically the number of stars in our analysis by applying that most probable value of  $A_I$  to the entire Orion locus sample. This is common practice in the study of open clusters, and given the low value of extinction that defines the peak in the spectroscopic  $A_I$  distribution, we are encouraged to use this technique in the outer ONC as well.

From Figure 7b we find that the width of the extinction peak has a  $\pm 1 \sigma$  value of 0.14 mag in  $A_I$ , which we take as the error in the mean extinction. Of the entire spectroscopic sample, 59% of the stars have  $A_I < 0.25$ , and 69% have  $A_I < 0.39$ , the modal value plus the  $1 \sigma$  width. Thus for nearly 70% of the stars, use of the modal extinction is assumed accurate at the 0.14 mag level in  $A_I$ . This  $A_I$  uncertainty translates into an uncertainty in  $E(V-I)$  of 0.08 and an uncertainty in  $E(U-V)$  of 0.12. These errors also propagate into formal uncertainties on stellar masses of  $\sim 0.03 M_\odot$  and on stellar ages of  $\sim 0.02$  dex (yr), which are discussed in § 5.1. (A discussion of the effect on UV excess and disk candidate selection appears in § 6.2.)

To minimize confusion about the effects of reddening in our conclusions, for the rest of this paper we will analyze the spectroscopic sample (using the best possible individual values of reddening) separately from the ensemble of combined photometric and spectroscopic data, using the most likely value of reddening,  $A_I = 0.25$ . For stars in the spectroscopic sample whose reddening is formally  $A_I < 0$ , we will simply set  $A_I = 0.25$ , keeping in mind that the latest M stars in particular might have incorrect reddening.

Figure 8 is the CMD for stars with spectra, dereddened on a star-by-star basis, resulting in an apparent quantization. Separately, the ensemble of photometry was dereddened by the most likely value of reddening; this CMD is not reproduced here, as it is identical to Figure 2, shifted by the most likely reddening vector as presented there. Figure 9 is the dereddened color-color diagram for the spectroscopic sample within the Orion locus. A plot of the ensemble photometry dereddened by the most likely reddening is again not presented, as it is essentially identical to Figure 3. There are many stars that are substantially bluer in  $U-V$

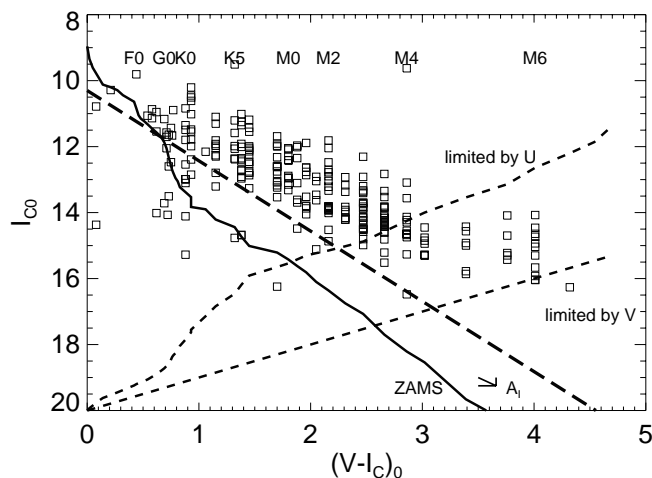


FIG. 8.—Dereddened CMD for stars with spectra. Notation is as in Fig. 2. The apparent quantization arises because stars are corrected to the colors expected based on their spectral type.

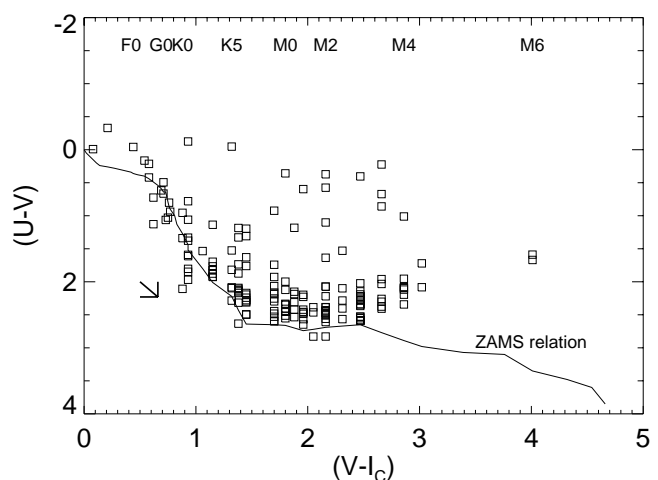


FIG. 9.—Dereddened color-color diagram for stars with spectra; notation is as in Fig. 3. The apparent quantization arises because stars are corrected to the  $V-I_C$  colors expected based on their spectral type. There are a significant number of stars well above the ZAMS relation showing  $U-V$  excesses.

compared with ZAMS counterparts, an effect that was apparent even before the reddening corrections.

## 5. CHARACTERISTICS OF THE ORION LOCUS SAMPLE

In this section we discuss the stellar age and mass distributions for the sample as a whole (§ 5.1), and we look for differences between the three fields studied (§ 5.2). We also discuss the stellar surface density (§ 5.3) in an attempt to understand how our sample stars are related to those populating the well-studied inner ONC.

### 5.1. Ages and Masses

The purpose of this section is not to derive definitive mass and age distributions, since selection effects and lack of membership information prohibit that; rather, we aim to understand the range of masses and ages sampled by our data set.

The models most often used in the analysis of PMS stars are those of D'Antona & Mazzitelli (1994, hereafter DAM), model 1 (Canuto & Mazzitelli convection prescription and Alexander opacities); these are the source of the isochrones and lines of constant mass plotted along with our dereddened data in Figure 10. Note that the ZAMS relation constructed from tabulated  $M_V$  and  $V-I_C$  values does not align well with the oldest isochrone. This is a result of a variety of factors, the largest being inaccuracies in models, since the discrepancy seems to remain under many different plausible transformations from the theoretical to the observational plane. We used the transformation from Hillenbrand (1997) in order to more easily enable comparisons with those data.

Based on the DAM grid of points, we interpolated masses and ages for our set of stars. We are unable to derive masses and ages for stars outside of the DAM grid, and so we have dropped these  $\sim 220$  apparently younger and lower mass stars from further analysis. The mass and age distributions for stars in the Orion locus are affected by the cut across the CMD to drop the field stars. Also, because it is only for the subsample of 1600 stars with  $U$ -band measurements that we can identify disk candidates and derive disk accretion rates

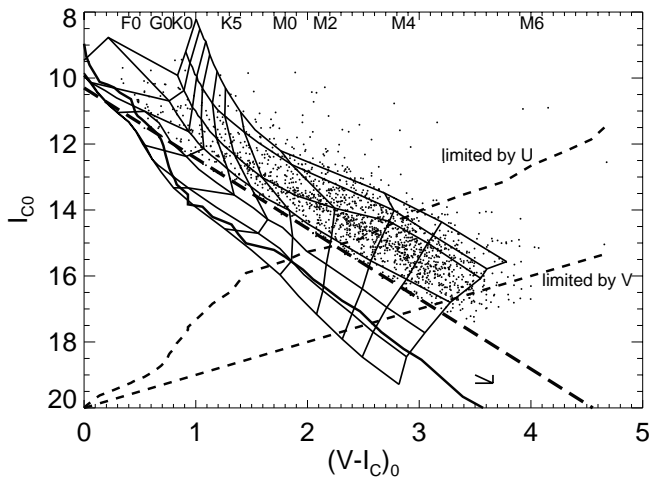


FIG. 10.—Dereddened CMD with all Orion locus stars plotted, with DAM model 1 isochrones and lines of constant mass (0.1, 0.3, 1, 3, 10, 30, and 100 Myr; 0.1, 0.15, 0.2, 0.3, 0.5, 0.7, 0.9, 1.2, 1.5, 2.0, and  $2.5 M_{\odot}$ ). All other notation is as in Fig. 2. Intersection of dashed detection limits and DAM model grid lines results in complicated completeness limits in terms of stellar mass and age; see text.

(compared with the 5000 with  $V$  and  $I$  measurements), we also consider how the  $U$ -limited mass and age distributions compare with the  $(V-I_C)$ -limited distributions. In what follows we account for these effects by plotting histograms of subsets of the data, with the ranges based on the intersection of lines and limits in Figure 10. The 3.0 Myr isochrone is very close to the line used to distinguish the Orion locus, and so represents the effective upper limit in age of our survey. For stars between 0.1 and 3 Myr, the  $U$  completeness limit intersects the 3 Myr isochrone at about  $0.30 M_{\odot}$ , but for stars younger than 1.0 Myr (but older than 0.1 Myr), we are complete in  $U$  to  $0.20 M_{\odot}$ . For the fainter  $V$  limit, we are complete between 0.1 and 3 Myr down to the lowest mass available,  $0.10 M_{\odot}$ . Our effective upper mass limit, restricted by brightness limits of our survey, is  $1.3 M_{\odot}$ . Since the reddening vector is essentially parallel to the isochrones, histograms of ages will be essentially unaffected by reddening uncertainties, while mass distributions will be moderately affected.

Figure 11 presents histograms of ages for several subsets of the Orion locus data. In each panel, the age span, mean age ( $10^6$  yr), and formal width ( $\pm 0.4$  dex) are identical. Also, in each of these cases, the histogram for the spectroscopic sample is statistically identical to the larger ensemble. The age and the age spread found here is consistent with that found for the inner ONC (Trapezium) region by Hillenbrand (1997), although there is some evidence that our population might be slightly older on average.

Figure 12 consists of similar histograms for the mass distributions. For most of the panels, the histogram for the spectroscopic sample is statistically identical to the larger ensemble. The only exception is the mass bin at  $\log M \sim 0.15$  in Figure 15c, in which the photometric sample is  $\sim 2 \sigma$  higher than the spectroscopic sample. This is an indication of the incompleteness of the spectroscopic sample at the lowest masses (reddest colors), which we have already recognized in Figure 6. That figure also suggested a slight overdensity at  $V-I_C \sim 1.5$  ( $M \sim 0.6 M_{\odot}$ ), but that overdensity evidently does not affect the mass distribution significantly.

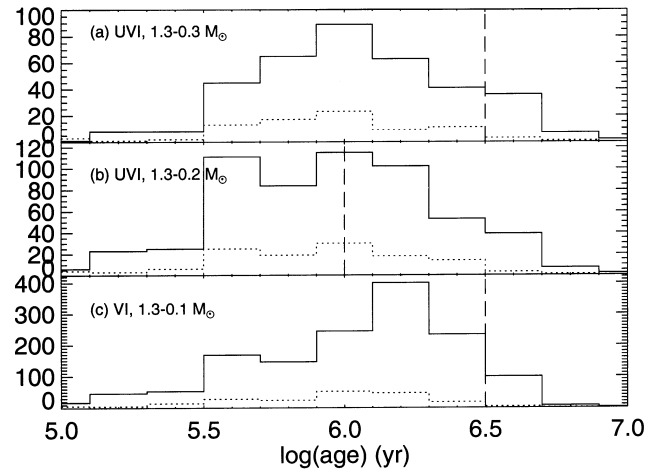


FIG. 11.—Histogram of ages for subsets of the data: (a)  $UVI_C$  data with  $0.3 M_{\odot} < M < 1.3 M_{\odot}$ , (b)  $UVI_C$  data with  $0.2 M_{\odot} < M < 1.3 M_{\odot}$ , and (c)  $VI_C$  data with  $0.1 M_{\odot} < M < 1.3 M_{\odot}$ . Solid lines are the ensemble of photometry (using most likely  $A_I$ ), and dotted lines are the spectroscopic sample (using specific  $A_I$ ). Vertical dashed lines denote approximate completeness limits; data are most complete to the left of the lines. In each panel, the mean age of the sample is identical at a value of  $6.0 \pm 0.4$  dex. Also, in each of these cases, the histogram for the spectroscopic sample is statistically identical to the larger ensemble.

## 5.2. Differences among the Fields

We invested some time using a variety of statistical tools to explore the similarities and differences between the stellar samples in our three fields. However, no robust differences with astrometric position were found in age, age spread, mass, UV excess (discussed below), or  $A_I$ . There are, as expected, parts of the sky that have a higher density of field stars (e.g., stars not in the Orion locus), and field 1 had by far the most field stars, by number and percent, of the three fields. Stellar surface density (see § 5.3) is the only parameter that differs significantly among the fields.

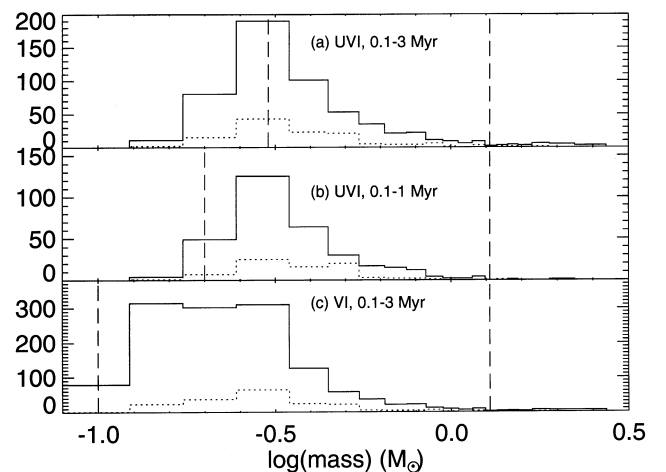


FIG. 12.—Histogram of masses for subsets of the data: (a)  $UVI_C$  data between 0.1 and 3 Myr, (b)  $UVI_C$  data between 0.1 and 1 Myr (with slightly different completeness limits in mass), and (c)  $VI_C$  data 0.1–3 Myr. Solid lines are the ensemble of photometry (using most likely  $A_I$ ), and dotted lines are the spectroscopic sample (using specific  $A_I$ ). Vertical dashed lines denote approximate completeness limits; data are most complete between the two lines. The histogram for the spectroscopic sample is statistically identical to the larger ensemble except for the mass bin at  $\sim 0.15 (M/M_{\odot})$  in panel (c); see text.



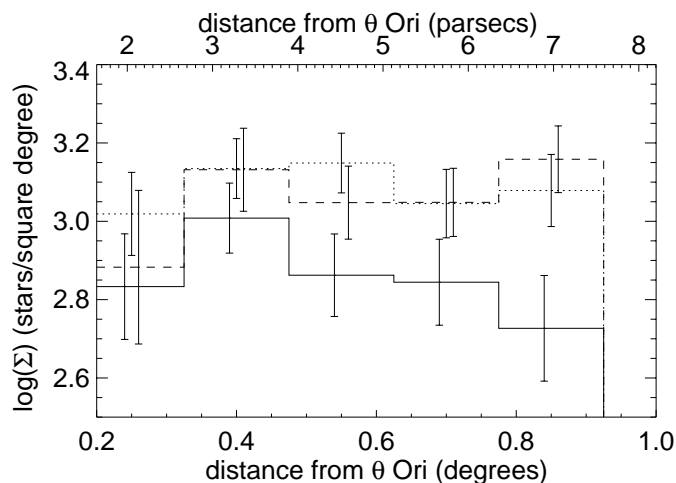


FIG. 13.—Surface densities: azimuthally integrated distribution of number of stars per square degree as a function of distance from  $\theta$  Ori for all three fields. Field 1 is the solid line, field 2 is the dotted line, and field 4 is the dashed line. These stellar-density profiles support the roughly north-south elliptical stellar surface density distribution found by HH.

### 5.3. Surface Density

Hillenbrand & Hartmann (1998, hereafter HH) find that azimuthally averaged stellar source counts in Trapezium are well fitted by King cluster models. Because our fields are more distant from  $\theta$  Ori, we are able to sample the stellar surface density farther out from the center of the cluster. Figure 13 is the azimuthally integrated distribution of number of Orion locus stars per square degree as a function of distance from  $\theta$  Ori for all three fields. Our innermost data overlap with the outermost data from HH, and the stellar densities are consistent with each other. The data from HH fall off fairly steeply; our data are consistent with a constant stellar density beyond that point, although some risk of field star contamination is still present in our data. Looking at the surface density falloff by individual field, fields 2 and 4 are essentially constant, but field 1, with the least nebosity of the three fields, falls off slightly, albeit still at a more shallow slope than that found by HH in the Trapezium region. These stellar density profiles support the roughly north-south elliptical stellar surface density distribution found by HH.

Not to be neglected, however, is the fact that the Orion Nebula Cluster is embedded in a foreground and background sample of young members of the general Orion Ic association. Because our data cover an area of  $1.6^\circ$  on the sky (up to  $0.8^\circ$  from  $\theta$  Ori), we potentially sample some of this Ic association in addition to the outer regions of the Orion Nebula Cluster.

## 6. DISK CANDIDATES

In this section, we discuss our procedure for identifying stars surrounded by circumstellar accretion disks. After presenting the range of UV excesses calculated from our data, we carefully select the minimum UV excess for defining a disk candidate. We then review the influence of factors that may provide false signatures of disks, including the effects of chromospheric activity, the use of a common “most likely” value of reddening for the ensemble of photometry, and the assignment of intrinsic colors to stars. In Appendix A, we investigate how our selection of disk candidates compares with IR candidate selection.

### 6.1. Measurement and Interpretation of UV Excess

We define UV excess as [dereddened  $(U - V)$ ] minus  $[(U - V)$  expected based on spectral type]; note that smaller values indicate it is bluer, so the more extreme a disk candidate, the more negative the UV excess. Figure 14 shows histograms of the UV excesses calculated for different sub-samples. For the photometric sample, the dereddened  $V - I_c$  value was used to determine the “expected”  $U - V$  from interpolation of the ZAMS relation; this ZAMS  $U - V$  was then compared with the observed dereddened  $U - V$  to determine a UV excess.

Each of the three distributions consists of a Gaussian, centered at about  $-0.3$  mag with width  $\sim 0.2$  mag, and a blue tail. The widths of the distributions are consistent with the net uncertainty from photometric errors, errors in spectral classification, and reddening uncertainties. The offset in the peak from zero is more ambiguous. Either all stars in our sample are accreting at a modest  $\dot{M}$  in the mean and so produce a small UV excess, or we have a systematic effect in our analysis that produces dereddened  $U - V$  colors slightly too blue. We explore possible reasons for this offset in the subsections below.

Based on the offsets from zero and the widths of these distributions, we choose a UV excess of  $-0.5$  mag to separate the Gaussian component from the blue tail component. We use this measure as the limit for distinguishing disk candidates from nondisk candidates in what follows. It is likely that our somewhat conservative choice excludes some bona fide disked stars. However, we feel that our limit must be well above the level of any systematic effects that may produce apparent UV excesses.

We show in Figures 15 and 16 color-color and color-magnitude diagrams of disk candidates selected based on UV excess. The spectroscopic and the ensemble photometric samples are shown separately. Note that the bulk of the UV-excess detections are for stars K5 and later, and that there is a wide distribution in dereddened  $V - I$  color of UV-excess stars.

We turn now to a discussion of the caveats associated with measuring a UV excess. These include the effects of using a common value of reddening for the ensemble of

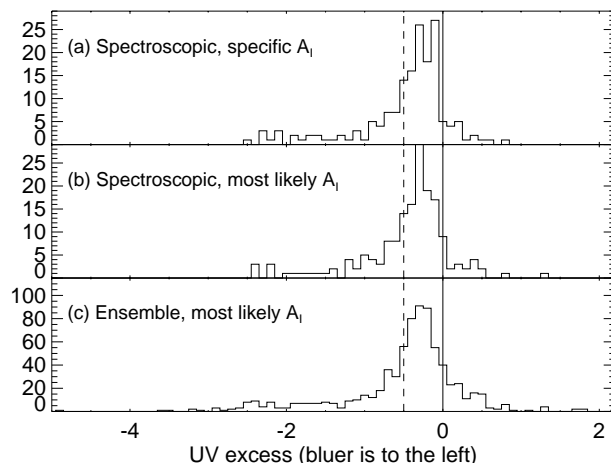


FIG. 14.—Histogram of calculated UV excesses. Smaller (more negative) UV excess is bluer. (a) Spectroscopic sample, using the specific  $A_I$  derived for each star; (b) spectroscopic sample, using  $A_I = 0.25$  for all stars; (c) entire ensemble of stars, using  $A_I = 0.25$  (note the different vertical scale). Stars to the left of the dashed lines at  $-0.5$  are selected as disk candidates. Positioning of dashed lines is discussed in the text.

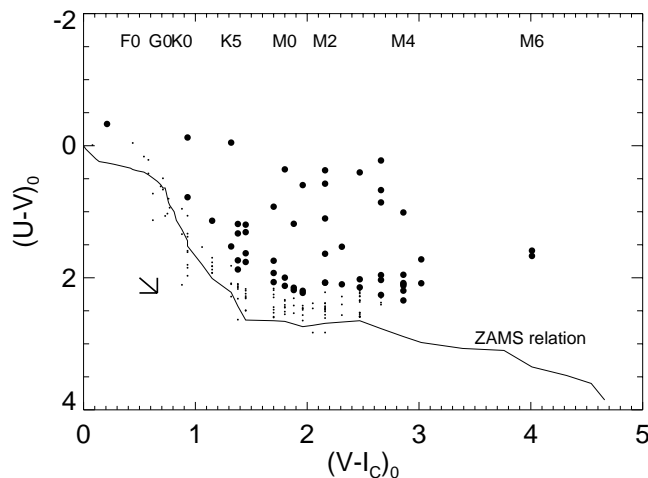


FIG. 15a

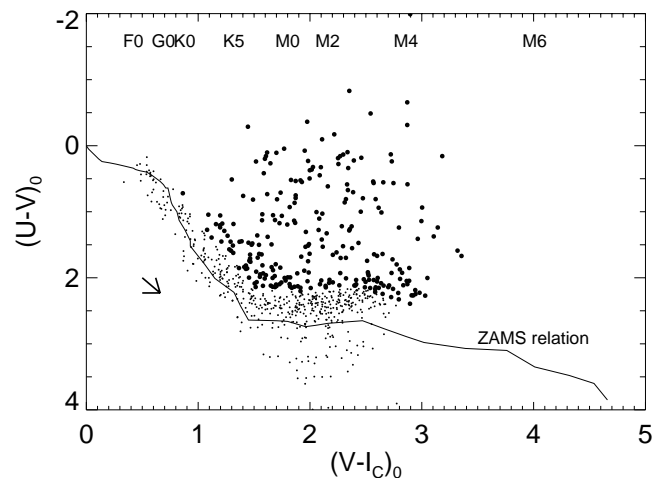


FIG. 15b

FIG. 15.—Dereddened color-color diagrams; the ZAMS relation is indicated, as is a most likely reddening vector. Stars that are identified as disk candidates are plotted as larger circles. (a) The spectroscopic sample, dereddened with values of  $A_I$  specific to each star; (b) the complete ensemble, dereddened by the most likely  $A_I$ . There are a still significant number of stars well above the ZAMS; stars below the ZAMS are likely background stars that have been undercorrected for extinction.

photometry, the effects of chromospheric activity, and the effects of uncertainties in the intrinsic stellar colors with which reddening-corrected colors are compared.

#### 6.2. Effects of Assuming a Common “Most Likely” Reddening

Calculation of UV excess is sensitive to the dereddening. Although we argued above (§ 4) that the peak in the spectroscopic extinction distribution could be interpreted within errors of 0.14 mag in  $A_I$  as the most likely extinction for the ensemble of photometry, we did not discuss the effects on determination of UV excess. Comparison of Figures 14a and 14b in Figure 14, shows that the aggregate difference is small between using the individual values of  $A_I$  and the most likely value of  $A_I = 0.25$ . These distributions are not

statistically different, with nearly identical widths and offsets from zero.

In Figure 17 we compare directly the UV-excess values obtained assuming the individual and the most likely extinction values. There is a good correlation, with 27 stars having UV excess larger than  $-0.5$  mag regardless of the extinction choice. Using the individual  $A_I$ -values, 36 stars are selected as disk candidates, and using the most likely value, 33 stars are selected; 82% of the disk candidates selected using the specific values of  $A_I$  are recovered using the most likely value of reddening. Note that the stars in the spectroscopic sample for which we derive an unphysical (negative)  $A_I$  have been dropped from this discussion. Including those stars does not change the overall result. We conclude that using the most likely value of reddening to

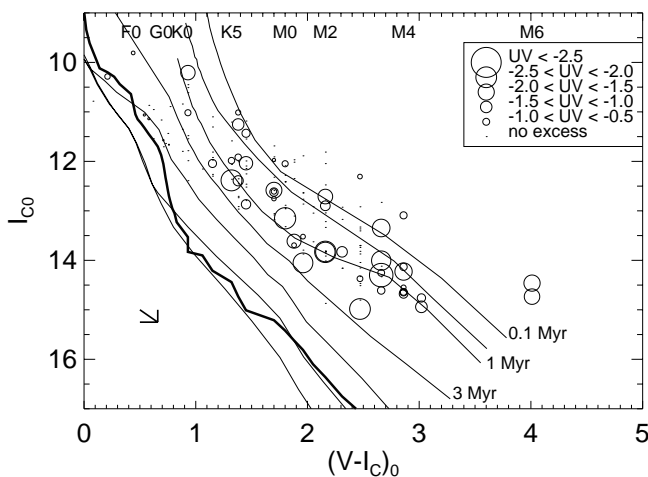


FIG. 16a

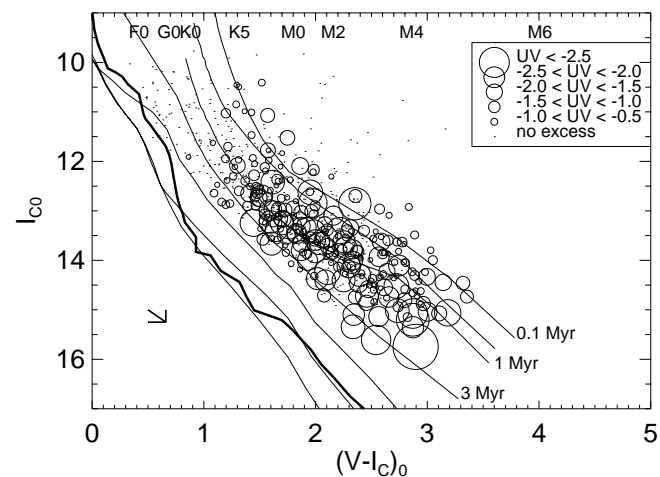


FIG. 16b

FIG. 16.—Dereddened CMD with disk candidates plotted as circles, where size of symbol corresponds to size of UV excess. (a) Spectroscopic sample dereddened using the specific extinction for each star; (b) ensemble dereddened using the mean extinction. All other notation is as in Fig. 2. Note that only  $UVI_C$  population is plotted, so there are few cool stars, and that the restriction to the population in the Orion locus limits the coverage of this diagram to stars above the 3 Myr isochrone, so the vertical scale is different than the other CMDs. DAM isochrones are plotted for 0.1, 0.3, 1, 3, 10, 30, and 100 Myr; isochrones (and the fact that they do not agree well with the ZAMS) are discussed in § 5.1. Disk candidates and the size of the UV excess are well distributed over the range of stars observed.

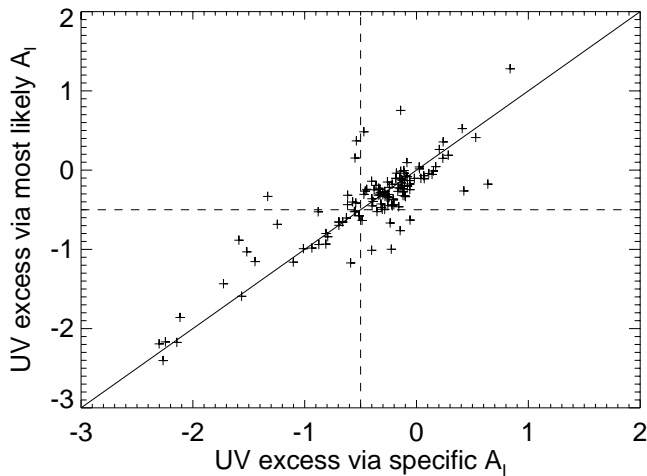


FIG. 17.—Implications of using the most likely reddening on the spectroscopic sample: comparison of UV excesses obtained using the individual  $A_I$  values (horizontal axis) with those obtained using the most likely value of  $A_I$  (vertical axis). Solid line: ideal case, no difference in derivations; dashed lines: disk selection limits of  $-0.5$ . Star counts in each quadrant: upper right, 86; lower right, 6; lower left, 27; upper left, 9. Eight percent of the stars selected as disk candidates using the specific values of  $A_I$  are recovered using the most likely value of reddening.

study the ensemble of photometry as a whole is valid in a statistical sense.

### 6.3. Effects of Chromospheric Activity

In this section we investigate the effects of chromospheric activity on the measured UV excesses by examining two distributions of stars: old solar neighborhood dMe stars, and young Taurus-Auriga stars that lack IR signatures indicative of disks.

#### 6.3.1. dMe Stars

One way to estimate the potential for contamination from a hot chromosphere is to look at the  $U-V$  excesses found for dMe stars in the solar neighborhood. We extracted the emission-line M stars from the Gliese & Jahreiss (1991) catalog, derived their  $U-V$  excesses using the same procedure as for the Orion locus data, and show the results in Figure 18a. Uncertainty in the assumed colors for (pre-main-sequence) stars of type M4 and later leads us to show in Figure 18b only stars earlier than M4. Based on these plots, we conclude that most chromospherically active stars have UV excesses smaller than our limit for disks of  $-0.5$  mag.

#### 6.3.2. Taurus-Auriga Stars

We used data presented in Kenyon & Hartmann (1995, hereafter KH) to determine the UV excesses for a sample of  $\sim 100$  stars in Taurus-Auriga, which we show in Figure 19. In addition to showing the distribution for all stars with UV and IR measurements, we separate out just those stars with positive IR disk indicators (CTTSs) and just those stars with no IR excess emission (WTTSs). The summed distribution of CTTSs and WTTSs is reminiscent of the UV excess distribution for our Orion locus sample (Fig. 14). We now see that the long blueward tail is largely populated by CTTSs showing IR signatures of disks, while the peak is largely populated by the nondisk WTTSs. Using our UV-excess criterion, 75% of the CTTSs are recovered, and only 10% of the WTTSs are selected. This statistic lends further

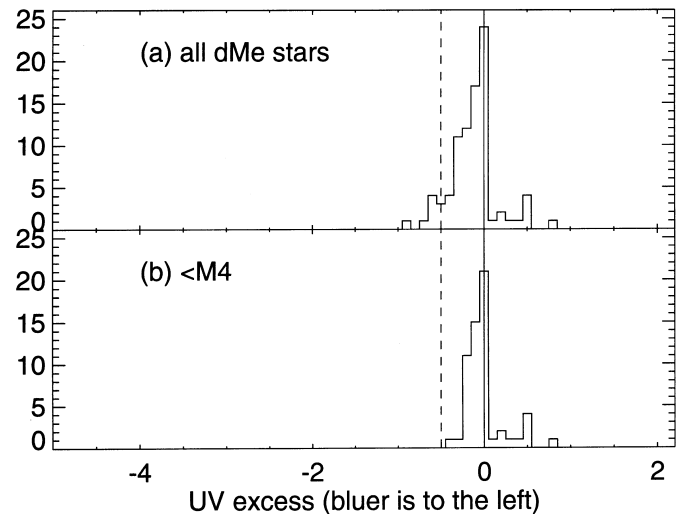


FIG. 18.—Histogram of UV excesses derived from dMe stars in the solar neighborhood (Gliese & Jahreiss 1991), plotted on the same horizontal scale as Fig. 14: (a) all dMe stars in catalog; (b) dMe stars earlier than M4. From this figure, we conclude that our disk indicator limit of  $-0.5$  mag in UV excess is not likely to include significant numbers of stars that are blue from chromospheric activity.

support for our selection of  $-0.5$  mag UV excess as a disk candidate limit. Further discussion of UV versus IR disk detection criteria appears in Appendix A. Even the slight offset from zero of the peak of the Taurus-Auriga UV excess distribution is similar to that seen in the Orion locus sample of Figure 14. This could reflect contributions from chromospheric activity or from the other uncertainties related to intrinsic colors, as we discuss in the next subsection. Finally, we note that there is a small red tail in all three distributions, Figures 14, 18, and 19. This too might be related to intrinsic color assignment.

### 6.4. Assignment of Intrinsic Colors

In addition to the effects just discussed (§§ 6.2 and 6.3) introduced by choice of dereddening technique and due to

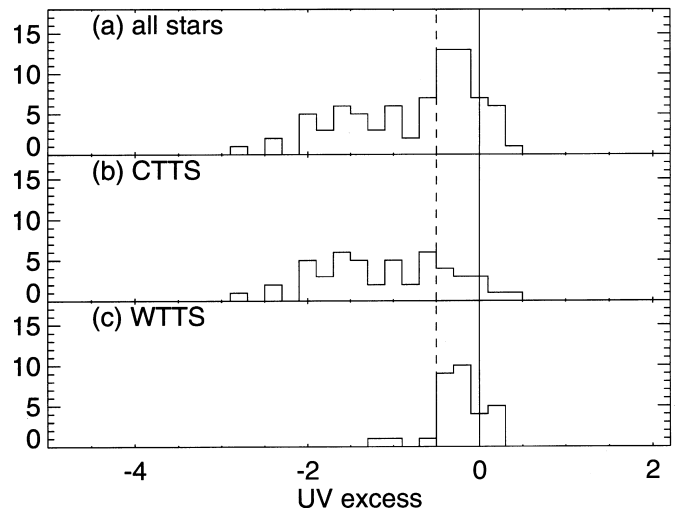


FIG. 19.—Histogram of UV excesses derived from stars in Taurus-Auriga (Kenyon & Hartmann 1995), illustrating the effect of (a) all stars in catalog with UV and IR measurements; (b) stars classified as CTTSs (disk candidates); (c) stars classified as WTTSs (nondisk candidates), illustrating the effect of our selection of  $-0.5$  mag UV excess as a disk candidate limit.

underlying chromospheric activity, there is one further point of detail relevant to the calculation of UV excess. There are systematic errors related to the actual intrinsic colors of young PMS stars and also spectral typing errors that become errors in the intrinsic colors we assume for the young PMS stars. These errors can, in turn, affect the calculated UV excesses, particularly at the latest spectral types.

1. *Intrinsic photospheric colors.*—There are reasons to suspect that the PMS  $V-I_C$  photospheric colors may be bluer than our assumed (ZAMS)  $V-I_C$  colors. The stars later than M4 are known to have the most uncertain ZAMS  $V-I_C$  colors, simply because observations of these faint stars are the most difficult to obtain. We consider three possible additional reasons that the assumed intrinsic photospheric colors may be wrong for these PMS stars: chromospheric activity, accretion activity, and the use of dwarf rather than giant colors.

a) *Chromospheric activity.*—Possibly these young, very late stars are simply bluer than expected due to more chromospheric activity than older stars of the same type. However, chromospheric activity alone is not likely to significantly affect the  $V-I_C$  colors (Houdebine et al. 1996).

b) *Accretion activity.*—We note that accretion activity can affect the observed  $V$  magnitude as well as the observed  $U$  magnitude; perhaps we are detecting accretion activity substantial enough to alter not only the  $U-V$  color but also the  $V-I_C$  color, which would make the observed  $V-I_C$  color bluer than expected. Since the latest stars have the coolest photospheres, it is possible that slight accretion activity can more easily pollute the  $V-I_C$  color in these stars. A much deeper sample (one that is known to be complete to types as late as M6) is required to investigate this possibility in detail. Within our sample, no correlation between derived reddening and UV excess was noted.

c) *Dwarf versus giant colors.*—It is possible that the assumed colors for the latest spectral types are simply systematically off. Although we have used the best possible values for the ZAMS (discussed in § 2.1, and identical to those found in Hillenbrand 1997), using older, bluer values for the lower main sequence, as tabulated by Straižys (1992), causes all of the reddenings to become positive. The fact that PMS stars have smaller gravities than dwarf stars (but larger than giants) might be a factor;  $V-I_C$  colors for giants are redder than those for dwarfs to about type M1, but are bluer than those for dwarfs below M1.

Let us consider the possibility that the true color scale is one intermediate between dwarf and giant stars. If so, the intrinsic  $V-I_C$  colors would be bluer than we assumed for the M stars, and redder for the G and K stars. How would the calculated values of UV excess change? For M stars, if the assumed  $V-I_C$  color is too red,  $A_I$  will be underestimated, and  $U-V$  will be undercorrected. Moreover, the assumed photospheric  $U-V$  will also be too red, and a disk candidate could be erroneously selected. For G and K stars, if the assumed  $V-I_C$  color is too blue, the effects are reversed, resulting in a disk candidate being lost. However, the intrinsic color uncertainty is smallest for the G and K stars, and this particular scenario is not likely to affect significantly our disk candidate selection in G and K stars. The color uncertainty in both  $V-I_C$  and  $U-V$  is greatest for the mid- to late-M stars, and hence the UV-excess calculations are more uncertain in this spectral type range.

2. *Systematic classification errors.*—The spectral classifications themselves have a degree of uncertainty. If a star is

classified incorrectly by a subclass (estimated mean error on our types; § 2.2), the size of the resultant color error is a strong function of spectral type (cf. ZAMS relation in Fig. 3). In  $V-I_C$ , G stars have a small error of only 0.01 (even for our estimated classification error of two subclasses), K stars have an error of  $\sim 0.1$ – $0.2$ , and M stars have errors that climb rapidly starting at 0.1 for the earliest types and growing to  $\gtrsim 0.4$  at the latest. In  $U-V$ , the error in G stars is  $\sim 0.05$ , in K stars  $\sim 0.2$ , and in M stars it flattens off to near 0 for the earlier types and 0.2 at the latest. If indeed stars are incorrectly classified, it is most likely that they are classified too early as a result of the effects of veiling filling in the lines, poor nebular subtraction, or both. If so, the assumed photospheric  $V-I_C$  color will be too blue, ultimately causing the loss of a potential disk candidate. In the case of the G and K stars, despite the fact that the types are more uncertain (two subclasses), the  $V-I_C$  colors do not change rapidly with type, although the  $U-V$  colors do. This error is in addition to the error in assumed intrinsic colors, so although the effects are likely to be small in the G and K stars, we are more likely to lose disk candidates than erroneously include them. For the M stars, the spectral types are more certain, half a subclass. If the star is erroneously classified too early, then the  $U-V$  will be overcorrected for reddening and compared with an intrinsic  $U-V$  that has not changed significantly; thus we will likely lose a real M star disk candidate. This effect is in the opposite direction as the color uncertainty, helping to offset it; however, the uncertainty in M star classification is probably less than the uncertainty in the intrinsic late M photospheric colors.

3. *Summary.*—In summary, for all spectral types considered (G, K, and M), we are more likely to lose real disk candidates than to include erroneous ones. In any case, the stars most subject to this color uncertainty are the stars redder than M4 ( $V-I_C > 2.86$ ), and, as it bears on disk candidate selection, very few of those are detected at all in  $U$ .

The  $V-I_C$  color uncertainty for late-type PMS stars is real; however, further investigation and clarification of the true photospheric colors for PMS stars is beyond the scope of this work. We have shown above that on the whole, it does not significantly affect the most likely reddening (§ 4); here we have shown that it also does not significantly affect the selection of disk candidates.

## 7. MASS ACCRETION RATES

In this section, we calculate mass accretion rates,  $\dot{M}$ , for the stars in our data set based on their  $U$ -band excesses (§ 7.1) and compare them with those derived by other authors using similar techniques in Taurus-Auriga (§ 7.2). We then investigate the implications of our survey sensitivity limits for the mass accretion rates (§ 7.3) and look for trends in accretion rates with stellar age and mass (§ 7.4), finding an absence of high  $\dot{M}$ -values among low-mass stars and among older stars.

### 7.1. Calculation of $\dot{M}$

We calculate mass accretion rates for our stars based on the excess emission at  $U$ , following the methods of Gullbring et al. (1998) and Hartmann et al. (1998). We start with dereddened photometry and tabulation of expected photospheric colors and assume a zero-magnitude flux ( $4.27 \times 10^{-9}$  ergs s $^{-1}$  cm $^{-2}$  Å $^{-1}$ ) for a  $U$ -filter bandwidth

(680 Å) as given by Gullbring et al. From this, we derive luminosities  $L_{U,\text{exp}}$  (from the expected photospheric color) and  $L_{U,0}$  (from dereddened magnitudes), which we compare to arrive at the excess luminosity in  $U$ .

Excess luminosity in  $U$  can be turned into total accretion luminosity,  $L_{\text{acc}}$ , via the formula derived by Gullbring et al.:

$$\log(L_{\text{acc}}/L_{\odot}) = 1.09 \log(L_{U,\text{ex}}/L_{\odot}) + 0.98,$$

where  $L_{U,\text{ex}} \equiv L_{U,0} - L_{U,\text{exp}}$ . Finally, we use the relation between  $\dot{M}$  and  $L_{\text{acc}}$  (also from Gullbring et al. and Hartmann et al.),

$$L_{\text{acc}} = 0.8 GM_* \dot{M}/R_*,$$

to calculate the mass accretion rate,  $\dot{M}$ . The factor of 0.8 accounts for the fact that the material is freely falling along the magnetosphere from a corotation radius of  $\sim 5 R_*$ . We derive  $M_*$  by interpolating the dereddened photometry between the DAM models. We derive  $R_*$  in the following manner: From the dereddened  $V-I_C$  colors, using formulae from Appendix C of Hillenbrand (1998), we derive  $T_{\text{eff}}$  and bolometric corrections for  $V$ , from which we derive the apparent bolometric magnitude for our stars. Using a distance modulus for Orion of 8.36 (Genzel et al. 1981; Walker 1969), we calculated the absolute bolometric magnitude. We can then derive  $L_{\text{tot}}$ :

$$\log(L_{\text{tot}}/L_{\odot}) = 0.4(4.75 - M_{\text{tot,abs}}),$$

where 4.75 is  $M_{\odot}$ . Since  $L_{\text{tot}} = 4\pi R_*^2 \sigma T_{\text{eff}}^4$ , we can calculate  $R_*$ . Combining all of this information, we can then derive a value of  $\dot{M}$  for each disk candidate.

### 7.2. Comparison with Taurus-Auriga

Gullbring et al. derive their formula relating  $L_{U,\text{ex}}$  and  $L_{\text{acc}}$  from stars ranging from K3–M4 in the Taurus-Auriga star-forming region, and Hartmann et al. apply this same formula to derive  $\dot{M}$  for stars between K6 and M2.5 in both the Taurus-Auriga and Chameleon star-forming regions. Data taken from the Hartmann et al. analysis of Taurus-Auriga are reproduced as plus signs in Figure 20. Mass accretion rates derived here (for Orion) are plotted as circles. The remainder of this figure will be discussed in the next section, but note for now that our range of  $V-I_C$  and  $\dot{M}$  overlaps well with the range of color and  $\dot{M}$  derived by Hartmann et al. Data from Hartmann et al. also overlap well with our range of masses and ages; they cover a mass range 0.25–0.9  $M_{\odot}$  and an age range  $10^{5-7.5}$ – $10^{7.5}$  yr, but we have dropped the four stars older than our maximum age  $10^{6.5}$  yr, restricting their data to the same range in age as our data.

### 7.3. Effective Limits in $\dot{M}$

Before correlating the  $\dot{M}$ -values with other values, e.g., stellar mass and age, we need to understand the selection effects inherent to our survey that limit our ability to find disk candidates at both the hot and cool extremes. From Figures 15 and 16, it is easy to see that the range of UV excesses exhibited increases as  $V-I_C$  increases; we find few disk candidates earlier than  $\sim K5$ , and essentially all of the stars fainter than our  $U$  cutoff are disk candidates. (The  $U$  cutoff was propagated into the CMD using ZAMS colors, and so the latest stars bright enough in  $U$  to be detected must be significantly brighter in  $U$  than the ZAMS counterpart; i.e., they are disk candidates.) We now wish to quan-

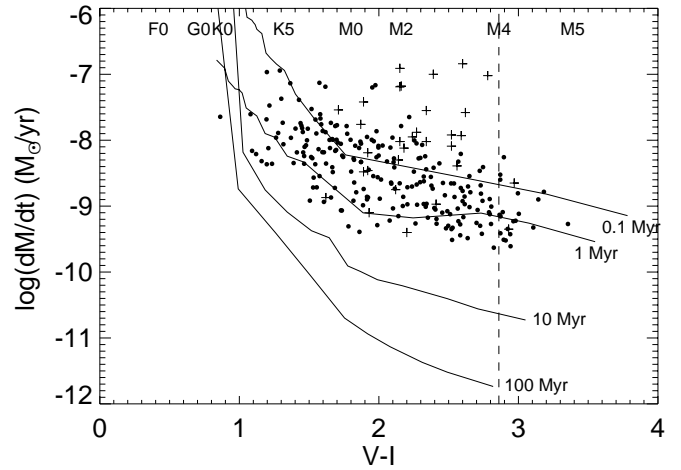


FIG. 20.—Mass accretion rates ( $\dot{M}$ ) and simple model calculations of minimum detectable  $\dot{M}$ . Solid lines correspond to minimum detectable  $\dot{M}$  for this simple model given limits for disk detection (UV excess bluer than  $-0.5$ ). Calculations were performed for the DAM grid of models, so lines correspond to age of 0.1, 1, 10, and 100 Myr. Note that we have dropped stars not in the Orion locus, including any older Orion members. Plus signs are data points from Hartmann et al. (1998) in Taurus-Auriga; circles are data from the photometric ensemble in this work. The vertical dashed line is provided to guide the eye toward the region of the diagram corresponding to types earlier than M4, where color uncertainties are minimized. The minimum detectable  $\dot{M}$  changes in a complex fashion as a function of many variables; see text.

tify our sensitivity to disk detection as a function of the stellar and the accretion properties.

In order to understand the strengths and limitations of our UV detections (and selection effects), we constructed some extremely simple models using the Buser & Kurucz (1992) stellar models to simulate stars (using the latest type provided, M1, as a proxy for all of the M stars tested) and an 8000 K blackbody of adjustable size superposed on the photosphere to simulate the accretion hot spot. For a range of stars and spot sizes, we solved this equation for the mass accretion rate,  $\dot{M}$ ,

$$L_{\text{spot}} = s(4\pi R_*^2) \sigma T_{\text{spot}}^4 \sim 0.8 GM_* \dot{M}/R_*,$$

where  $s$  is the fraction of stellar surface covered by the spot(s). We calculated  $U-V$  excesses (as in § 6.1) for a range of spot sizes and for a range of stellar temperatures and luminosities corresponding to the range covered by the DAM models and by our data and determined the  $s$  that corresponds to a marginal detection for each of the grid points.<sup>10</sup> A marginal detection is defined by our limits for disk candidate selection as established above, ( $U-V$ ) bluer than  $-0.5$  mag and well in excess of any source of random or systematic error. Based on these marginal detection values, we then calculated the corresponding  $\dot{M}$  limits.

Results of these simulations are summarized in Figures 20, 21, and 22. We stress that our models are simple and that they are meant to demonstrate only the general trends of how the minimum detectable  $\dot{M}$  changes in a complex fashion as a function of many variables, not specifically what that  $\dot{M}$ -value is. Looking first at the overall trends in

<sup>10</sup> Phenomenologically, of course, we are putting a limit on  $sT_{\text{spot}}^4$ , not just  $s$ , but since these are not sophisticated models and since the purpose of these simple models is to understand how all these effects interact, we have opted to keep the models simple and just modify  $s$ , keeping  $T_{\text{spot}}$  constant.

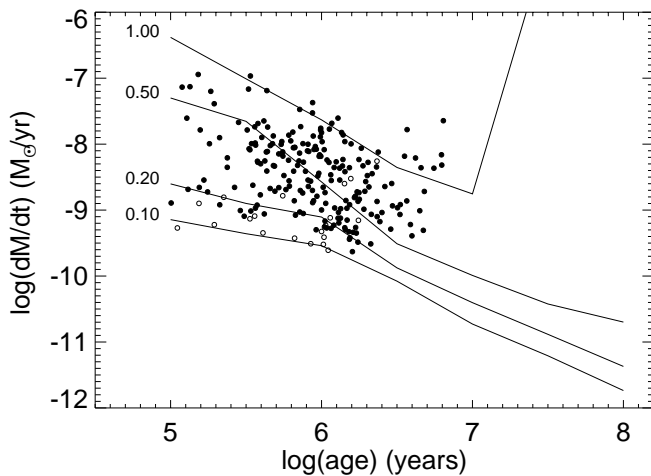


FIG. 21.—Another view of the simple model calculations of minimum detectable  $\dot{M}$  for this simple model. As in Fig. 20, solid lines correspond to minimum detectable  $\dot{M}$  given limits for disk detection. Lines correspond to masses of 0.10, 0.20, 0.50, and  $1.00 M_{\odot}$  as marked. Circles are data from the photometric ensemble in this work; filled circles correspond to stars with  $(V-I_C) < 2.86$ . The minimum detectable  $\dot{M}$  changes in a complex fashion as a function of many variables; see text. Note the absence of stars with age greater than 1 Myr and  $\dot{M} > 10^{-8} M_{\odot} \text{ yr}^{-1}$ .

the solid lines in Figure 20, for types earlier than G–K, the star is sufficiently hot that addition of an 8000 K spot does not make much detectable difference in the calculated  $U$  magnitude; for even earlier types, the addition of a spot is not detectable within the simulation to the limits of numerical noise. Moving to cooler stars, the contrast between the stellar photosphere and the accretion hot spot increases, and the spot becomes increasingly easier to detect.

Recall that colors are most uncertain for types M4 ( $V-I_C > 2.86$ ) and later; this corresponds to the vertical dashed line. To minimize the influence of the color uncertainties, stars with colors redder than 2.86 will be differentiated in the plots that follow. This does not rule out the possibility that those stars we detect later than M4 might still be legitimate disk candidates, but simply makes interpretation of the subsequent analysis more straightforward.

Figures 21 and 22 are additional views of these simple models with our data overplotted, for age and mass, respectively. As above, the selection effects are complicated. In the next section, we investigate the trends present in our data, keeping in mind these approximate trends in detection limits. Selected lines from these models will be carried over into subsequent plots.

#### 7.4. $\dot{M}$ Trends with Stellar Mass and Age

In order to investigate trends of  $\dot{M}$  with stellar age and mass, we must be careful to isolate the variable of interest from any of the systematic trends of  $\dot{M}$  detectability just outlined. Hartmann et al. (1998) find trends of  $\dot{M}$  versus age, and as can be seen in Figure 20 we are sensitive to the same range of  $\dot{M}$ -values. However, their disk candidates were IR-selected and thus may be subtly different than our UV-selected sample despite the results of Appendix A. Certainly the role of detection limits is different in our case because, in our case, UV itself is used as a disk indicator.

Figure 23 shows  $\dot{M}$  versus age for several subsets of the data. The limits in age and mass for  $\dot{M}$  measurement as established earlier in the age histograms, Figures 11a and

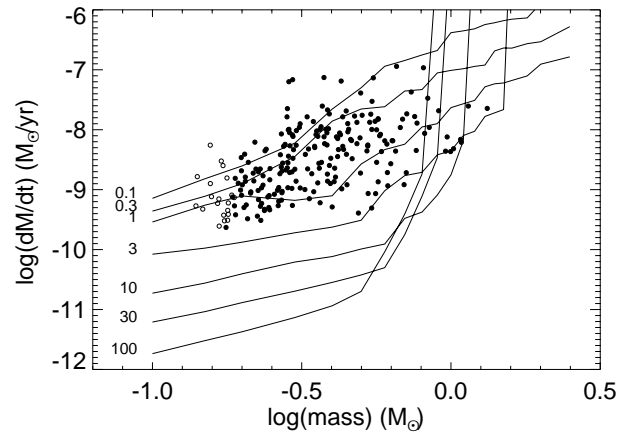


FIG. 22.—A third view of the simple model calculations of minimum detectable  $\dot{M}$  for this simple model. As in Fig. 20, solid lines correspond to minimum detectable  $\dot{M}$  given limits for disk detection. Lines correspond to ages 0.1, 0.3, 1, 3, 10, and 100 Myr as indicated. Circles are data from the photometric ensemble in this work; filled circles correspond to stars with  $(V-I_C) < 2.86$ . The minimum detectable  $\dot{M}$  changes in a complex fashion as a function of many variables; see text. Note the absence of stars with  $M < 0.3 M_{\odot}$  and  $\dot{M} > 10^{-8.5} M_{\odot} \text{ yr}^{-1}$ .

11b, are also used here for the photometric ensemble in Figures 23a and 23b; Figure 23c is the spectroscopic sample. We have shown in § 3 that the spectroscopic sample is representative of the photometric sample within the Orion locus, and here it is most useful to interpret trends

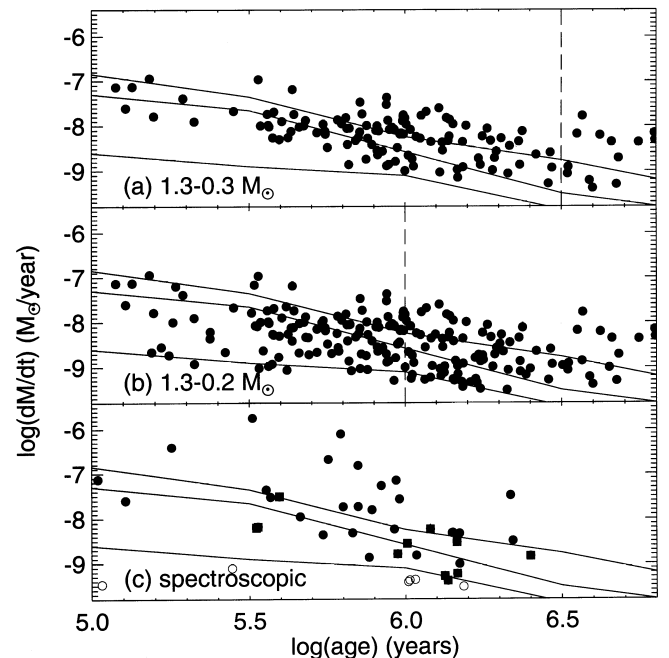


FIG. 23.—Values of  $\dot{M}$  derived via Gullbring et al. (1998) plotted vs. age (a) for the photometric ensemble with  $0.3 M_{\odot} < M < 1.3 M_{\odot}$ , (b) for the photometric ensemble with  $0.2 M_{\odot} < M < 1.3 M_{\odot}$ , and (c) for the spectroscopic sample. In all three panels, dashed lines are completeness limits from Fig. 11 (data more complete to the left of the lines), and solid lines are detection limits from Fig. 21 for 0.7, 0.5, and  $0.2 M_{\odot}$  (top to bottom). In (c), open circles are stars with  $(V-I_C) \geq 2.86$ , and squares are the stars with  $0.2 M_{\odot} < M < 0.3 M_{\odot}$ ; for comparison with (a), omit the squares, and for comparison with (b), include them. There are no stars with  $(V-I_C) \geq 2.86$  that are within the stated mass ranges for the ensemble. Star counts in each panel: (a) 116, (b) 180, (c) 44. Although any trends found in these data may be masked by selection effects, the lack of older stars with higher accretion rates is real.

using the plots with considerably more stars. There are a few stars with higher  $\dot{M}$  in the spectroscopic sample, as a result of better values of  $A_I$  for a few stars. This is expected based on the assumptions we made about the  $A_I$  distribution.

These data appear to show systematic trends, but certainly at the lower envelope, this is driven by the detection limits. The upper envelope, however, suggests a lack of low-mass stars with high  $\dot{M}$ .

Recall that the significantly larger population of stars (at similar masses and ages) without a UV excess or for which we could not measure a  $U$  magnitude necessarily constitutes a population of stars with accretion rates that are much less than those seen in Figure 23. The interaction of all of the selection effects and sensitivity issues results in the brightest candidates (those with highest  $\dot{M}$ ) being more readily detected in each age bin and an overall trend that resembles the detection limits. However, Figure 11 reveals explicitly how many stars were observed to contribute to the final selection of disk candidates. For example, in Figure 11c,  $\sim 400$  stars are observed (most with  $U$  below our threshold) between ages  $10^{6.1}$  and  $10^{6.3}$  to produce the  $\sim 30$  stars with  $U$  excesses plotted in Figure 23b. *Although we should be sensitive to stars with  $\dot{M} \sim 10^{-7.5}$  at ages  $\sim 10^{6.3}$  in Figure 23a, we do not see them. This hole is still present in Figure 23b, but the completeness limit prevents us from drawing any firm conclusions. In Figure 23c, the spectroscopic sample,  $\dot{M}$  overall is generally larger than those obtained for the ensemble, but there is still a lack of older stars with higher  $\dot{M}$ . Although any trends found in this data may be masked by selection effects, this lack of older stars with higher accretion rates is real.*

We can also investigate the relationship between  $\dot{M}$  and stellar mass (see Fig. 24). As before, the limits in age and mass as established in the mass histograms, Figures 12a and 12b, are also used for the photometric ensemble here in Figures 24a and 24b; Figure 24c is the spectroscopic sample. As with the trend against age above, the spectroscopic sample overall has higher mass accretion rates than the photometric ensemble.

As in the correlation with age, the lower envelope of the data tracks the detection limits, and the upper envelope of the data is not as sensitive to the detection limits. We are still detecting only the brightest stars in each range of masses, but note that *we should be sensitive to stars of  $\log(M) \sim -0.65$  with accretion rates  $\gtrsim 10^{-7.5}$ , but we do not see them.* There are more than 400 stars observed in  $VI_C$  (most with  $U$  below our threshold) with  $-0.8 < \log(M) < -0.6$ , and none of them have  $\dot{M} > 10^{-7.5}$ . *The lack of stars with high accretion rates and low masses is real and not an observational artifact.*

In conclusion, although we should be sensitive to stars with high  $\dot{M}$  and ages 1–3 Myr, we do not see them, nor do we see stars with high  $\dot{M}$  and low masses. Although the selection effects are complicated, we believe the lack of stars in these ranges is real and indicates the presence of real characteristics of the change of  $\dot{M}$  with stellar age and mass.

### 7.5. Accretion Disk Fraction

The oldest, youngest, and range of ages of the accretion disk candidates are all of interest for exploring the range of disk lifetimes and evolution of disks and, ultimately, the development of planetary systems. However, the complicated selection effects as a function of age and mass and the

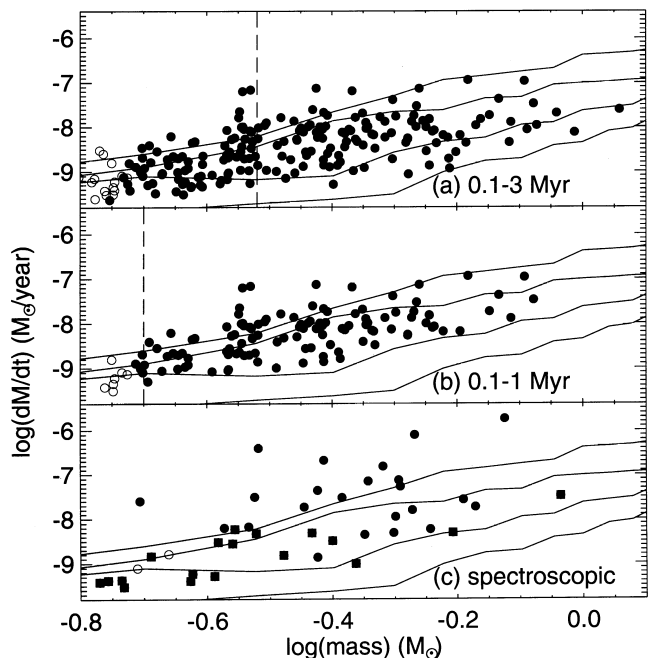


FIG. 24.—Values of  $\dot{M}$  derived via Gullbring et al. (1998) plotted vs. mass (a) for the photometric ensemble between 0.1 and 3 Myr, (b) for the photometric ensemble between 0.1 and 1 Myr, and (c) for the spectroscopic sample. In all three panels, open circles are stars with  $V-I_C \geq 2.86$ , dashed lines are completeness limits from Fig. 12 (data more complete to the right of the lines), and solid lines are detection limits from Fig. 22 for 0.1, 0.3, 1, and 3 Myr (top to bottom). In (c), squares are the stars between 1 and 3 Myr; for comparison with (a), include the squares, and for comparison with (b), omit them. Star counts in each panel: (a) 197, (b) 109, (c) 44. Although any trends found in these data may be masked by selection effects, the lack of stars with high accretion rates and low masses is real.

limited membership information restrict our ability to calculate an accretion disk fraction. Strictly speaking, any disk fractions we calculate are lower limits to the true disk fraction.

As can be seen in Figure 16, there are some stars that are slightly younger than  $10^5$  yr with UV excesses, some quite large, but none much younger than the youngest isochrone. (Recall that we cannot formally find ages or masses for stars outside the DAM grid.) The oldest members of Orion, of course, are lost by the cutoff used to separate the Orion locus from the field stars. The oldest accretion disk candidates we find, however, are comparable in age to the oldest stars without UV excesses above the field star cutoff.

The fraction of accretion disk candidates for stars within the DAM grid is  $\sim 0.40$  and is constant over several bins of age, mass, and radial distance from  $\theta$  Ori. Hillenbrand et al. (1998), using IR disk detection methods, investigated disk fraction as a function of distance from  $\theta$  Ori; these data, constrained in a similar fashion to our data, result in comparable disk fractions in the range of distances where we overlap ( $\sim 1.5$ – $2.5$  pc).

## 8. CONCLUSIONS

In this study of the Orion Nebula Cluster flanking fields, we have come to the following major conclusions.

1. Based on DAM ages, the mean age and age spread of our sample is  $6.0 \pm 0.4$  dex, consistent with but possibly older than the ages of stars in the Trapezium region reported by Hillenbrand (1997).

2. We find disk candidates at all ages and masses of our sample. The fraction of disk candidates is approximately constant at  $\sim 40\%$  for a range of masses and ages but is strictly a lower limit to the true disk fraction.

3. By constructing some simple models, we determined our approximate effective minimum detectable  $\dot{M}$  as a function of  $V - I_C$ , age, and mass. Accretion is not detectable for the earliest types/largest masses. Lower accretion rates are detectable for older lower mass stars than younger lower mass stars.

4. Despite these complicated selection effects, which mask overall trends in  $\dot{M}$  with mass and age, we derive a trend with age that is consistent with that found for Taurus-Auriga by Hartmann et al. (1998) and a trend with mass that is consistent with that found for higher masses by Hillenbrand et al. (1992).

5. Again, despite these complicated selection effects, there are stars with certain characteristics to which we should be sensitive, but which we do not see. We do not see stars with high  $\dot{M}$  and ages 1–3 Myr, nor do we see stars with high  $\dot{M}$  and masses  $0.2\text{--}0.3 M_\odot$ . In this context, “high  $\dot{M}$ ” refers to rates comparable to those obtained elsewhere in our distribution,  $\log \dot{M} \sim -8$  to  $-7.5$ , although the absolute value of the accretion rate is likely to be subject to systematic uncertainties; for example, using different reddening values changes the range of  $\dot{M}$  obtained, but the “holes” in the diagrams remain.

6. The stellar surface density falls off faster with distance from  $\theta$  Ori (the center of Trapezium) in field 1 and is essentially constant in fields 2 and 4, supporting the roughly

north-south elliptical stellar surface density distribution found by Hillenbrand & Hartmann (1998) for the Trapezium region.

7. We expected to find differences among the three fields studied, but they are remarkably identical in many ways, including age, age spread, and mass, UV excess, and  $A_I$  distributions. The only way in which they significantly differ is in stellar surface density.

Light curves and their interpretation for most of these targets will be presented in a forthcoming study (Rebull 2000).

We wish to thank the anonymous referee for extensive comments on the original manuscript. We also wish to thank the WIYN-queue observers for obtaining the data for our program. This research has made extensive use of NASA’s Astrophysics Data System Abstract Service. The Digitized Sky Surveys, used in Figure 1, were produced at the Space Telescope Science Institute under grant NAGW-2166. The images of these surveys are based on photographic data obtained using the Oschin Schmidt telescope on Palomar Mountain and the UK Schmidt telescope. The plates were processed into the present compressed digital form with the permission of these institutions. L. A. H. acknowledges research support from NASA Origins of Solar Systems grant NAG 5-7501. S. E. S. also acknowledges support from the NASA Origins Program. L. M. R. would like to thank NOAO for enabling trips to Tucson.

## APPENDIX A

### UV VERSUS IR DISK DETECTION

Having established our UV disk detection limit and investigated several implications of this limit, the question naturally arises of how to compare our UV-based survey results with that of more common IR disk surveys. KH present optical and infrared colors for stars in Taurus-Auriga, and these data allow us to investigate the use of UV versus IR disk detection.

After investigating several color indexes, KH conclude that  $K - L$  provides the most robust discrimination to distinguish WTTS (with no accretion disk indicators) from CTTS (with accretion disk indicators). Since  $L$ -band measurements are often difficult to obtain,  $H - K$  is also frequently used as a disk indicator. More recently, Hillenbrand et al. (1998) in their study of stars in the Trapezium region used  $I_C - K$  excess as a disk indicator. Excesses for all of these color indexes are calculated in a manner similar to that used in this paper to calculate  $U - V$  excess. For completeness, here we compare the use of UV excess to  $K - L$  excess,  $H - K$  excess, and  $I_C - K$  excess as disk indicators.

Of the data presented from Taurus-Auriga in KH, there are  $\sim 80$  stars with  $UVIHK$  data between types K0 and M4. We applied our analysis as described above to determine UV excess, which is plotted against  $K - L$  excess in Figure 25a, against  $H - K$  excess in Figure 25b, and against  $I_C - K$  excess in Figure 25c.

Of the stars selected as disk candidates using an IR method, 76% of stars showing a  $K - L$  excess are recovered using the UV method, 77% of stars showing a  $H - K$  excess are recovered, and 65% with an  $I_C - K$  excess are recovered. The stars that are selected as disk candidates based on UV excess but not based on IR methods are likely to be stars with an unfavorable inclination or large disk holes or both. Stars that are selected as disk candidates based on IR methods but not UV excess may have low accretion rates or incorrect reddening corrections.

## APPENDIX B

### Ca AND H $\alpha$

In other studies, disk candidate identification has been done from H $\alpha$  surveys. Although our classification spectra include the Ca II infrared triplet and H $\alpha$ , we are not confident in H $\alpha$  as an additional disk diagnostic, because in the ONC there is substantial nebular emission at H $\alpha$ ; it cannot be relied upon in the absence of other indicators to diagnose active accretion or disk presence or both. The Ca IR triplet has also been discussed as a disk indicator (Hillenbrand et al. 1998), and equivalent



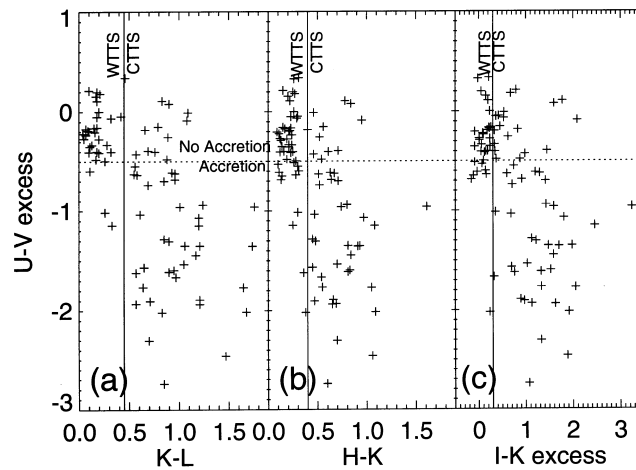


FIG. 25.—Comparison of IR and UV disk indicators, based on data from Taurus found in KH. The dashed horizontal line is the UV excess limit established for disk candidates,  $-0.5$ . In (a)  $K-L$  excess greater than  $0.30$  constitutes a disk candidate; in (b)  $H-K$  excess greater than  $0.2$  constitutes a disk candidate; in (c)  $I_C-K$  excess greater than  $0.3$  constitutes a disk candidate. All methods find most of the disk candidates. Star counts in each quadrant, clockwise from upper right-hand corner: (a) 12, 37, 3, 28; (b) 10, 34, 11, 33; (c) 19, 36, 9, 24.

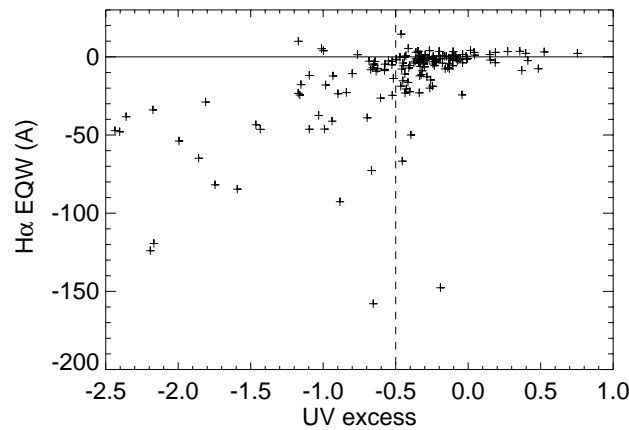


FIG. 26.—Mean equivalent width for nebula-subtracted  $H\alpha$  plotted against UV excess. The dashed vertical line corresponds to disk candidate selection limit. Measurement of lines was not possible for every classifiable spectrum, but the stars with the largest UV excesses also tend to have  $H\alpha$  in strong emission.

widths have even been used to determine mass accretion rates (Muzerolle et al. 1998). Our resolution is insufficient to use the Ca lines in this fashion, and there is additional confusion with nebular H emission in the Paschen series.

In Figure 26 we show that the stars with the largest UV excesses also tend to have  $H\alpha$  in strong emission. We plot only stars for which we are able to measure equivalent widths; there are several others for which such measurements are not possible either because of low signal-to-noise ratio or because the lines are filled in to the level of the continuum. We conclude that UV excess is a more reliable indicator of disk presence than Ca II or  $H\alpha$  equivalent width.

#### REFERENCES

- Allen, L. E., & Strom, S. E. 1995, *AJ*, 109, 1379  
 Basri, G., & Bertout, C. 1989, *ApJ*, 341, 340  
 Bertout, C., Basri, G., & Bouvier, J. 1988, *ApJ*, 330, 350  
 Bessell, M. S. 1991, *AJ*, 101, 662  
 Buser, R., & Kurucz, R. L. 1992, *A&A*, 264, 557  
 Calvet, N., Hartmann, L., & Strom, S. E. 2000, in *Protostars and Planets IV*, ed. V. Mannings, A. P. Boss, & S. S. Russell (Tucson: Univ. Arizona Press)  
 D'Antona, F., & Mazzitelli, I. 1994, *ApJS*, 90, 467 (DAM)  
 Fitzpatrick, E. L. 1999, *PASP*, 111, 63  
 Genzel, R., Reid, M. J., Moran, J. M., & Downes, D. 1981, *ApJ*, 244, 884  
 Gliese, W., & Jahreiss, H. 1991, *Third Catalogue of Nearby Stars* (Preliminary Version), in *Selected Astronomical Catalogs, Vol. 1* (ADC/NSSDC CD-ROM) (Greenbelt, MD: GSFC)  
 Gullbring, E., Hartmann, L., Briceño, C., & Calvet, N. 1998, *ApJ*, 492, 323  
 Haro, G., & Herbig, G. H. 1955, *Bol. Obs. Tonantzintla & Tacubaya*, No. 12, 33  
 Hartigan, P., Kenyon, R., Hartmann, L., Strom, S. E., Edwards, S., Welty, A. E., & Stauffer, J. 1991, *ApJ*, 382, 617  
 Hartmann, L. 1998, *Accretion Processes in Star Formation* (Cambridge: Cambridge Univ. Press)  
 Hartmann, L., Calvet, N., Gullbring, E., & D'Alessio, P. 1998, *ApJ*, 495, 385  
 Herbst, W., Rhode, K. L., Hillenbrand, L. A., & Curran, G. 2000, *AJ*, 119, 261  
 Hillenbrand, L. A. 1997, *AJ*, 113, 1733  
 Hillenbrand, L. A., & Hartmann, L. 1998, *ApJ*, 492, 540 (HH)  
 Hillenbrand, L. A., Strom, S. E., Calvet, N., Merrill, K. M., Gatley, I., Makidon, R., Meyer, M., & Skrutskie, M. F. 1998, *AJ*, 116, 1816  
 Hillenbrand, L. A., Strom, S. E., Vrba, F. J., & Keene, J. 1992, *ApJ*, 397, 613  
 Hollenbach, D. J., Yorke, H. W., & Johnstone, D. 2000, in *Protostars and Planets IV*, ed. V. Mannings, A. P. Boss, & S. S. Russell (Tucson: Univ. Arizona Press)  
 Houdebine, E. R., Mathioudakis, M., Doyle, J. G., & Foing, B. H. 1996, *A&A*, 305, 209  
 Jones, B. F., & Walker, M. F. 1988, *AJ*, 95, 1755  
 Kenyon, S. J., & Hartmann, L. 1995, *ApJS*, 101, 117 (KM)  
 Kirkpatrick, J. D., Henry, T. J., & McCarthy, D. W. 1991, *ApJS*, 77, 417

- Landolt, A. U. 1992, *AJ*, 104, 340  
Lasker, B. M., et al. 1988, *ApJS*, 68, 1  
Leggett, S. K. 1992, *ApJS*, 82, 351  
Leggett, S. K., Allard, F., & Hauschildt, P. H. 1998, *ApJ*, 509, 836  
McNamara, B., Hack, W. J., Olson, R. W., & Mathieu, R. D. 1989, *AJ*, 97, 1427  
Muzerolle, J., Hartmann, L., & Calvet, N. 1998, *AJ*, 116, 455  
Najita, J. R., Edwards, S., Basri, G., & Carr, J. 2000, in *Protostars and Planets IV*, ed. V. Mannings, A. P. Boss & S. S. Russell (Tucson: Univ. Arizona Press)  
Parenago, P. P. 1954, *Tr. Gos. Astron. Inst. Stenberga*, 25, 1  
Rebull, L. 2000, in preparation  
Stassun, K. G., Mathieu, R. D., Mazeh, T., & Vrba, F. J. 1999, *AJ*, 117, 2941  
Straizys, V. 1992, *Multicolor Stellar Photometry* (Tucson: Pachart)  
Tian, K. P., van Leeuwen, F., Zhao, J. L., & Su, C. G. 1996, *A&AS*, 118, 503  
van Altena, W. F., Lee, J. T., Lee, J.-F., Lu, P. K., & Upgren, A. R. 1988, *AJ*, 95, 1744  
Walker, M. F. 1956, *ApJS*, 2, 365  
———. 1969, *ApJ*, 155, 447  
Walter, F. M., Vrba, F. J., Mathieu, R. D., Brown, A., & Myers, P. C. 1994, *AJ*, 107, 692